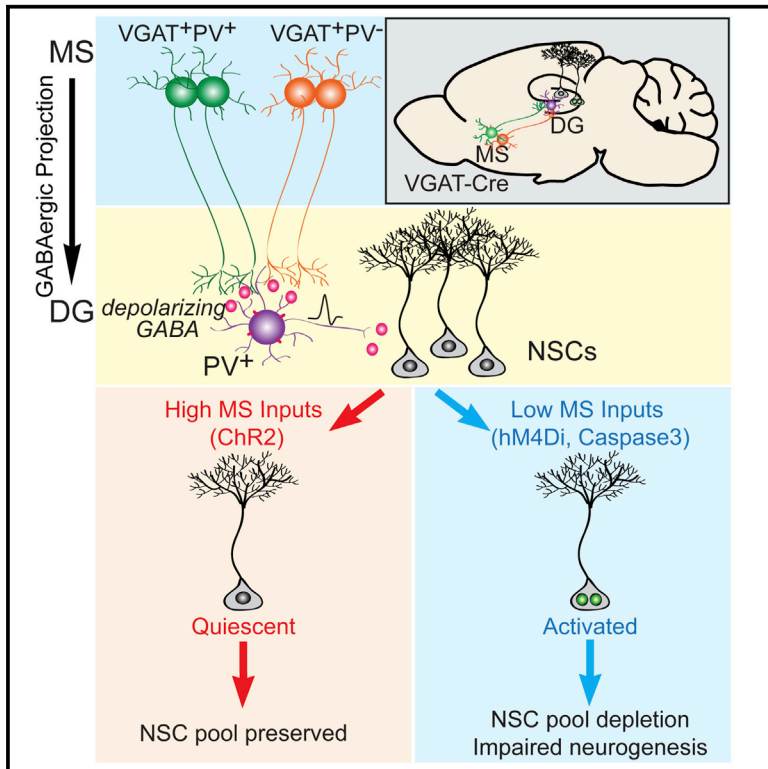


Long-Range GABAergic Inputs Regulate Neural Stem Cell Quiescence and Control Adult Hippocampal Neurogenesis

Graphical Abstract



Authors

Hechen Bao, Brent Asrican, Weidong Li, ..., Karl Deisseroth, Benjamin Philpot, Juan Song

Correspondence

juansong@email.unc.edu

In Brief

Bao et al. demonstrate that long-range GABAergic projections from the medial septum control adult hippocampal neurogenesis through depolarizing GABA signaling onto local PV interneurons. Functionally, these long-range inputs are required for maintaining NSC quiescence and ablating them depletes the NSC pool and impairs neurogenesis.

Highlights

- GABA neurons from the medial septum (MS) synapse with dentate PV interneurons
- Dentate PV interneurons couple MS projections to NSCs via depolarizing GABA signals
- MS GABA projection neurons regulate NSC quiescence and activation
- Ablating MS GABA neurons depletes the NSC pool and impairs neurogenesis



Long-Range GABAergic Inputs Regulate Neural Stem Cell Quiescence and Control Adult Hippocampal Neurogenesis

Hechen Bao,^{1,2,7} Brent Asrican,^{2,7} Weidong Li,^{1,7} Bin Gu,³ Zhexing Wen,⁵ Szu-Aun Lim,² Isaac Haniff,² Charu Ramakrishnan,⁶ Karl Deisseroth,⁶ Benjamin Philpot,^{3,4} and Juan Song^{2,4,8,*}

¹Bio-X Institutes, Brain Science and Technology Research Center, Shanghai Jiao Tong University, Shanghai 200240, China

²Department of Pharmacology, University of North Carolina, Chapel Hill, NC 27599, USA

³Department of Cell Biology and Physiology, University of North Carolina, Chapel Hill, NC 27599, USA

⁴Neuroscience Center, University of North Carolina, Chapel Hill, NC 27599, USA

⁵Department of Psychiatry and Behavioral Science, Emory University, Atlanta, GA 30322, USA

⁶Department of Bioengineering, Stanford University, Stanford, CA 94305, USA

⁷These authors contributed equally

⁸Lead Contact

*Correspondence: juansong@email.unc.edu

<https://doi.org/10.1016/j.stem.2017.10.003>

SUMMARY

The quiescence of adult neural stem cells (NSCs) is regulated by local parvalbumin (PV) interneurons within the dentate gyrus (DG). Little is known about how local PV interneurons communicate with distal brain regions to regulate NSCs and hippocampal neurogenesis. Here, we identify GABAergic projection neurons from the medial septum (MS) as the major afferents to dentate PV interneurons. Surprisingly, dentate PV interneurons are depolarized by GABA signaling, which is in sharp contrast to most mature neurons hyperpolarized by GABA. Functionally, these long-range GABAergic inputs are necessary and sufficient to maintain adult NSC quiescence and ablating them leads to NSC activation and subsequent depletion of the NSC pool. Taken together, these findings delineate a GABAergic network involving long-range GABAergic projection neurons and local PV interneurons that couples dynamic brain activity to the neurogenic niche in controlling NSC quiescence and hippocampal neurogenesis.

INTRODUCTION

The adult mammalian brain is a dynamic structure, capable of remodeling in response to various environmental stimuli. One dramatic example of brain plasticity is the birth and subsequent integration of newborn neurons into the existing circuitry of the adult brain. Dentate gyrus (DG) granule neurons are continuously generated from neural stem cells (NSCs) within the adult hippocampus throughout life in all mammals including human. Upon neurogenic division, multipotent adult NSCs give rise to neural precursors, which in turn become immature neurons and integrate into the existing neural circuit to become mature granule neurons. Substantial evidence sug-

gests that adult-born granule neurons participate in specific brain functions, including learning and memory, stress responses, and mood regulation (Harrison, 2004; Kempermann et al., 2008; Le Strat et al., 2009; Zhou et al., 2013). In sharp contrast to embryonic neurogenesis, regulation by neuronal activity is a hallmark of adult neurogenesis (Kriegstein and Alvarez-Buylla, 2009; Ming and Song, 2011; Zhao et al., 2008). Physiological or pathological stimuli, presumably acting upon specific neuronal networks, regulate distinct stages of adult neurogenesis (Ming and Song, 2011; Song et al., 2012a, 2012b; Zhao et al., 2008). Identification of the neuronal networks regulating adult NSCs and neurogenesis is fundamentally important yet challenging due to lack of information on the network connections linking distal brain regions to the neurogenic regions. Our recent studies demonstrated that dentate parvalbumin (PV)-expressing interneurons, among several other interneuron cell types, serve as a unique local circuit component to regulate adult NSCs and their progeny through GABA signaling (Song et al., 2012b, 2013). These studies highlight the critical roles of local circuits in regulating adult NSCs and hippocampal neurogenesis. We wondered whether dentate PV interneurons, as a local niche component, communicate with distal brain regions in order to relay environmental information to the neurogenic niche to regulate NSCs and hippocampal neurogenesis.

Here, using rabies-virus-based monosynaptic retrograde tracing, we identified medial septum (MS) GABAergic neurons as the major afferents to the dentate PV interneurons. Functionally, these long-range GABAergic inputs are both necessary and sufficient to maintain the quiescence of adult NSCs. Strikingly, NSC regulation by MS GABAergic neurons is mediated by depolarizing GABA signaling onto dentate PV interneurons. This is in sharp contrast to most mature neurons in the adult brain where GABA acts as a hyperpolarizing neurotransmitter (Ben-Ari, 2002; Owens and Kriegstein, 2002). Chronic ablation of MS GABA neurons and their projections leads to stem cell pool depletion and impaired neurogenesis. Therefore, our study identifies a GABAergic network with region and cell type specificity that couples distal brain activity to the neurogenic niche to

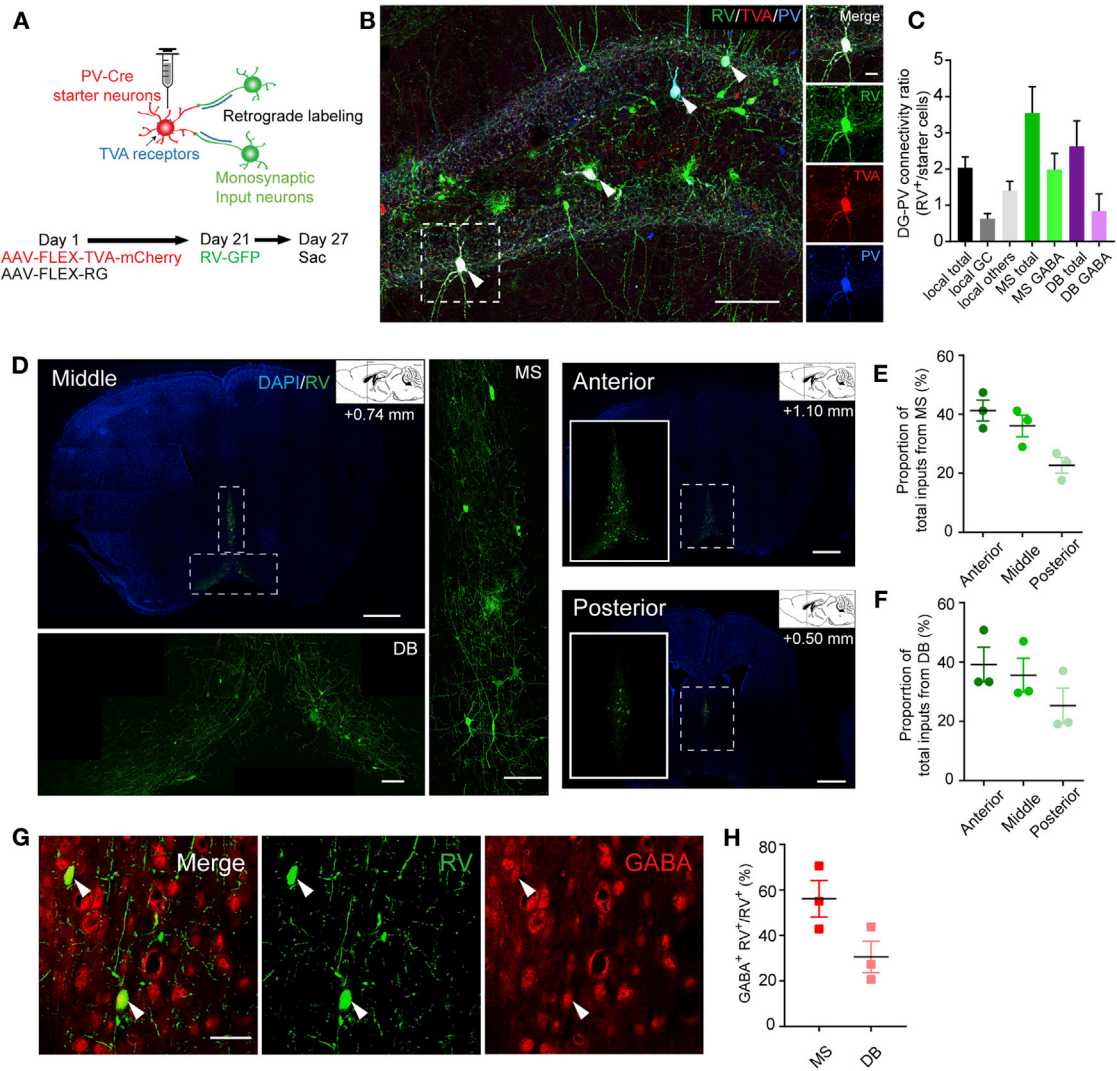


Figure 1. Dentate PV Interneurons Receive Monosynaptic GABAergic Inputs from the MS and DB

(A) Experimental scheme of monosynaptic retrograde rabies tracing in the DG of PV-cre animals. (B) Composite confocal images showing the starter PV neurons in DG (arrowheads). Scale bar, 100 μ m (left) and 20 μ m (right). (C) Connectivity ratio of DG-PV interneurons to different brain regions ($n = 3$). GC, granule cell; MS, medial septum; DB, diagonal band of Broca. (D) Composite confocal images showing RV input neurons in regions of the MS and DB ($n = 3$). Scale bar, 1 mm (coronal) and 100 μ m (zoomed in). (E) Distribution of RV input neurons in the MS ($n = 3$). (F) Distribution of RV input neurons in the DB ($n = 3$). (G) Confocal images showing input neurons in the MS colocalized with GABA marker. Arrow heads pointing to GABA⁺ RV⁺ cells. Scale bar, 50 μ m. (H) Percentage of GABA⁺ RV⁺ out of total input cells in the MS and DB ($n = 3$). Values represent mean \pm SEM. See also [Figure S1](#).

regulate the quiescence of NSCs, the maintenance of NSC pool, and hippocampal neurogenesis.

RESULTS

Dentate PV Interneurons Receive Major GABAergic Inputs from the MS and Diagonal Band Complex

To identify the afferents to dentate PV interneurons, we used a rabies-virus (RV)-based approach for retrograde tracing of monosynaptic inputs (Miyamichi et al., 2011; Wall et al., 2013; Watabe-Uchida et al., 2012; Wickersham et al., 2007). First, we

expressed avian-specific retroviral vector TVA and rabies glycoprotein (RG) specifically in the dentate PV cells by unilaterally injecting two Cre-dependent AAV vectors (AAV-FLEX-TVA-mCherry and AAV-FLEX-RG) to the DG of PV-Cre mice. Three weeks later, the same mice received unilateral microinjections of the pseudotyped RV-GFP into the same region of the DG, and mice were sacrificed 6 days after RV injection (Figure 1A). We validated that our injection site was restricted to the DG (Figure S1A) and that the starter cells labeled by TVA-mCherry and RV-GFP were PV immunopositive (Figure 1B). Control animals that received Cre-dependent mCherry (AAV-FLEX-mCherry)

and RG (AAV-FLEX-RG) along with RV exhibited absence of labeling of starter cells and presynaptic inputs (Figure S1B). These results therefore confirmed that transsynaptic action of RV is dependent on the expression of TVA in the starter cells. Whole-brain distributions of presynaptic inputs to dentate PV neurons were examined and aligned based on Allen Institute's reference atlas (Lein et al., 2007). Our results revealed input neurons predominantly in the MS and the diagonal band of Broca (DB) (Figures 1C, 1D, and S1A). Our quantification revealed that the great majority of the afferent inputs come from the anterior and middle subregions (Unal et al., 2015) of the MS and the DB (Figures 1E and 1F). Furthermore, we found that 56% of all RV-labeled neurons in the MS were immunopositive for GABA, in comparison to only 31% in the DB (Figures 1G and 1H), suggesting that MS GABAergic projections are the major afferents to dentate PV interneurons. Consistent with this, we found that the other two major neuron populations in the MS, the cholinergic (ChAT⁺) and glutamatergic (VGLUT2⁺) neurons, do not send projections to the neurogenic region (Figures S1C–S1F). We therefore selectively targeted GABAergic neurons in the MS for further investigation.

VGAT^{MS-DG} Projections Functionally Interact with Quiescent NSCs through Dentate PV Interneurons

As MS GABAergic neurons are the major inputs to dentate PV interneurons, we sought to identify the projection pattern of MS GABAergic neurons in the DG. We injected Cre-dependent AAV-expressing YFP (AAV-DIO-YFP) to the MS of VGAT-Cre mice (Vong et al., 2011) to selectively label GABAergic neurons (Figures 2A, 2B, and S2A) and examined the projections in the DG. Confocal imaging revealed prominent MS projections to the DG subgranular zone (SGZ) and hilus (Figure 2C) and complex baskets around the PV cell bodies (Figure 2D). Importantly, MS axonal terminals on the dentate PV interneurons express the presynaptic marker synapsin1 (Figure S2B). Next, we sought to determine synaptic properties of these VGAT^{MS-DG} projections using Channelrhodopsin2 (ChR2)-assisted circuitry mapping in acute brain slices (Petreanu et al., 2007; Weissbourd et al., 2014). We generated VGAT-Cre::PV-Flp double-transgenic mice in order to independently label VGAT neurons in the MS and PV neurons in the DG (Figure 2E). Specifically, we delivered a Cre-dependent AAV-expressing ChR2-mCherry (AAV-DIO-ChR2-mCherry) to the MS, and a Flp-dependent AAV-fDIO-YFP to the DG. We validated the specificity of PV-Flp mouse line in labeling PV neurons in the DG (Figures S2C and S2D). Whole-cell recordings of dentate PV interneurons exhibited postsynaptic currents (PSCs) upon optogenetic activation of VGAT^{MS-DG} projections (Figures 2F and 2G). These responses were completely blocked by the GABA_A receptor antagonist bicuculline (Figures 2F and 2G). As septo-hippocampal GABAergic neurons form synapses onto multiple interneuron types in the hippocampus (Freund and Antal, 1988), and local interneurons are potentially interconnected (Armstrong and Soltesz, 2012), we examined the latency of evoked PSCs in PV neurons in response to light stimulation of VGAT^{MS-DG} projections. At ~3 ms (Figure S2E), these light-evoked PSCs likely represented monosynaptic connections, as polysynaptic connections normally have a much longer latency of ~7 ms (Kohara et al., 2014).

To determine whether VGAT^{MS-DG} projections functionally interact with radial NSCs (rNSCs), we generated VGAT-Cre::Nestin-GFP double-transgenic mice (Figure 2H). We injected Cre-dependent AAVs expressing either mCherry or ChR2-mCherry into the MS to label GABAergic neurons. Confocal imaging showed no close associations between mCherry VGAT^{MS-DG} projections and NSCs (Figure 2I). We then recorded GFP⁺ rNSCs and found that optogenetic activation of VGAT^{MS-DG} projections induced a slow tonic baseline shift (≥ 4 pA) (Figure 2J), indicative of indirect rather than direct VGAT^{MS-DG} connections. Since rNSCs lack functional synapses (Tozuka et al., 2005), they likely respond to GABA spillover from nearby synapses (Moss and Toni, 2013; Song et al., 2012b). Previous studies using electron microscopy demonstrated that septo-hippocampal GABAergic projections selectively innervate hippocampal interneurons, not mature principle cells (Freund and Antal, 1988). Consistent with this, we failed to observe light-evoked PSCs in mature GCs upon optogenetic stimulation of VGAT^{MS-DG} projections (Figure S2F). We hypothesized that light-evoked slow tonic GABA currents are mediated by local PV interneurons. We recorded rNSCs upon light stimulation of VGAT^{MS-DG} projections in the presence or absence of ω -Agatoxin TK that specifically blocks P/Q type calcium channels unique to PV⁺ interneurons (Hefft and Jonas, 2005; Wilson et al., 2001) and observed that ω -Agatoxin largely abolished the light-evoked slow tonic GABA component (Figures 2J and 2K). Importantly, failure to respond to light stimulation of VGAT^{MS-DG} projections was not due to an unhealthy state of the NSCs, as they subsequently responded to muscimol (Figure S2G), indicating intact GABA_ARs. Together, these data suggest that VGAT^{MS-DG} projections functionally interact with quiescent NSCs through dentate PV interneurons.

Activity of VGAT^{MS-DG} Projections Bi-directionally Regulates the Quiescence of NSCs

Next, we assessed the functional impact of VGAT^{MS-DG} projections on rNSCs *in vivo*. To specifically activate VGAT^{MS-DG} projections, we used a previously established *in vivo* optogenetic approach (Song et al., 2012b, 2013). We injected Cre-dependent AAV-DIO-YFP or ChR2-YFP into the MS of adult VGAT-Cre mice. An optical fiber above the DG specifically restricted activation to only distal VGAT^{MS-DG} projections (Figure 3A). PV cells reliably followed a train of 10-Hz light stimulation of VGAT^{MS-DG} projections (Figure 3B). We then utilized an *in vivo* light paradigm to activate VGAT^{MS-DG} projections followed by labeling of proliferating cells with thymidine analogue 5-ethynyl-2'-deoxyuridine (EdU) (Figure 3C). To rule out the possibility of light artifact on neurogenesis, the same light stimulation paradigm was used on VGAT-Cre mice injected with Cre-dependent YFP control virus. Activated NSCs were identified as SGZ cells containing nestin⁺ radial processes and EdU incorporation (Figure 3D). *In vivo* optogenetic stimulation significantly reduced EdU incorporation (Figure 3E) in rNSCs without affecting neural progenitors (Figure 3F) or nestin⁺ NSC pool size (Figure 3G). Surprisingly, the decrease in NSC activation occurred significantly at the ventral (but not dorsal) blade of the DG (Figure S3A), suggesting regional control of NSC activation/quiescence states by the MS-DG GABAergic pathway. To rule out the possibility of circuit adaptations associated with a 5-day light paradigm, we tested a much shorter light paradigm with only 8-hr light stimulation

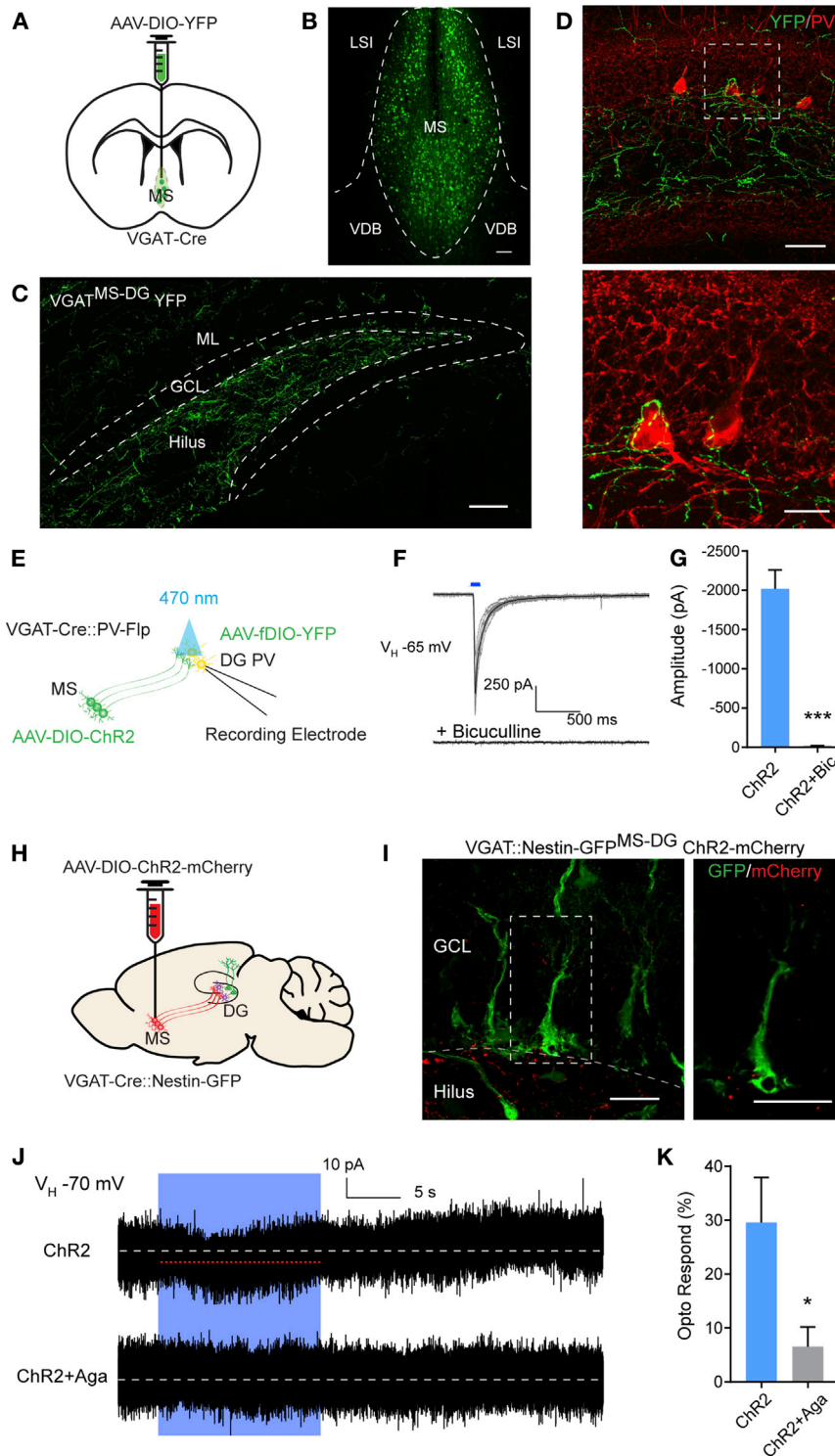


Figure 2. VGAT^{MS-DG} Projections Functionally Interact with Quiescent NSCs through Dentate PV Interneurons

(A) AAV-DIO-YFP injection scheme to the MS of VGAT-Cre mice.

(B) Composite confocal image showing selective targeting of the MS GABAergic neurons in VGAT-Cre mice. MS, medial septum; LSI, lateral septum intermediate; VDB, ventral diagonal band.

(C) Composite confocal image of prominent MS VGAT projections to the SGZ and hilus. GCL, granule cell layer; ML, molecular layer. Scale bar, 100 μ m.

(D) Axonal collaterals from MS GABA cells closely associate with the soma of dentate PV interneurons. Scale bar, 50 μ m (top) and 20 μ m (bottom).

(E) Schematic illustration for patch-clamp recording of dentate PV cells in response to light stimulation of VGAT^{MS-DG} projections in acute brain slices from VGAT-Cre::PV-Flp double-transgenic mice.

(F) Overlaid traces showing whole-cell recordings of a dentate PV cell responding to blue light of VGAT^{MS-DG} projections expressing Chr2. Black line indicates a single example trace. Responses were blocked by bicuculline.

(G) Average amplitude of light evoked postsynaptic currents from dentate PV cells in the absence and presence of bicuculline (n = 3 cells with total 25 trials for Chr2, and 10 trials for Chr2+Bicuculline).

(H) AAV-DIO-ChR2-mCherry injection scheme to the MS of VGAT-Cre::Nestin-GFP double-transgenic mice.

(I) No association between VGAT^{MS-DG} projections and GFP⁺ rNSCs. Scale bar, 50 μ m (left) and 20 μ m (right).

(J) Whole-cell voltage-clamp recording of GFP⁺ rNSC upon light stimulation of ChR2-expressing VGAT^{MS-DG} projections (top trace). Identical recording as above, but in the presence of ω -Agatoxin TK to block P/Q type Ca²⁺ channels specific to PV interneurons (bottom trace). White dotted line is mean baseline level; red line highlights the small inward deflection during the light stimulation.

(K) Probability of detecting light-evoked responses for the two recording conditions depicted in Figure 2J. Trials with mean deflection \geq 4 pA are considered responding to light stimulation (n = 5). *p < 0.05, ***p < 0.001 by Student's t test.

Values represent mean \pm SEM. See also Figure S2.

(30 s every 5 min). Our results showed that 8-hr light stimulation also decreased activation of rNSCs to a similar extent as the 5-day light paradigm (Figure 3B), suggesting that no significant circuit adaptation had occurred.

For *in vivo* inhibition of VGAT^{MS-DG} projections, a chemogenetic approach would avoid long-term light-induced damage

to brain tissues. Cre-dependent AAVs expressing mCherry or the inhibitory designer receptor exclusively activated by designer drug (DREADD) hM4Di-mCherry were injected to the MS of adult VGAT-Cre mice. Clozapine-N-oxide (CNO) was locally infused via a guide cannula to the dentate to selectively inhibit VGAT^{MS-DG} projections (Figure 3H) (Figure 3I). Electrophysiology recordings validated hM4Di reduction in frequency (not amplitude) of spontaneous inhibitory postsynaptic currents (sIPSCs) in dentate PV

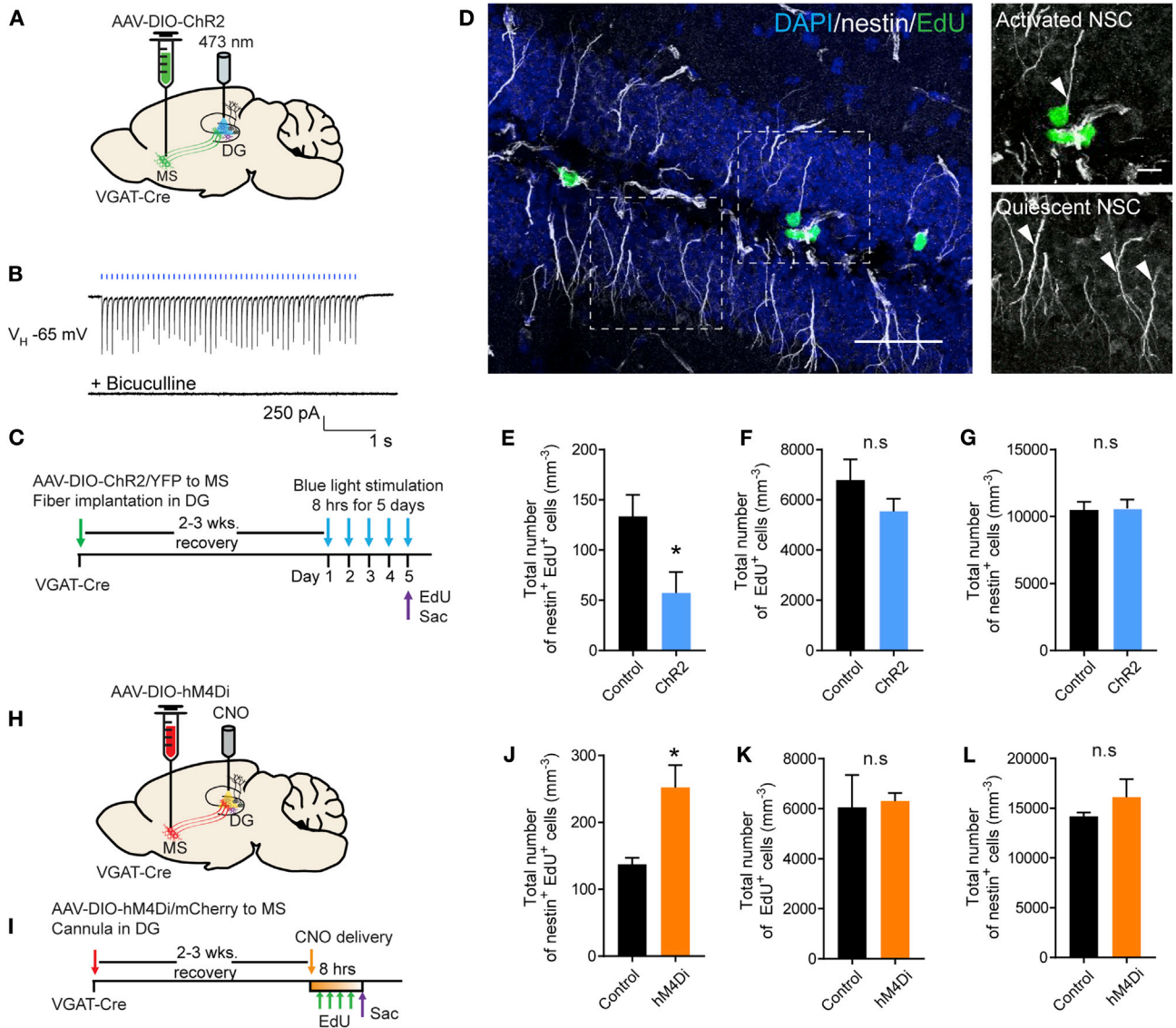


Figure 3. Activity of VGAT^{MS-DG} Projections Bi-directionally Regulates Quiescence/Activation of NSCs

(A) AAV-DIO-Chr2-YFP injection scheme to the MS and projections from MS to DG in the VGAT-Cre mice.
 (B) Trace showing dentate PV cells reliably follow a 10-Hz train of 1-ms, 470-nm light stimulation of VGAT^{MS-DG} projections without synaptic failures. Synaptic responses were blocked by bicuculline.
 (C) Experimental paradigm for *in vivo* optogenetic stimulation.
 (D) Composite confocal images showing quiescent (nestin⁺EdU⁻) and activated (nestin⁺EdU⁺) rNSCs. Scale bar, 50 μ m (left) and 10 μ m (right zoomed in).
 (E–G) Density of activated rNSC (nestin⁺EdU⁺) (E), proliferating cells (EdU⁺) (F), and the rNSC pool (nestin⁺) (G) (n = 8 for control, and n = 6 for Chr2).
 (H) AAV-DIO-hM4Di-mCherry injection scheme to the MS and projections from MS to DG in the VGAT-Cre mice.
 (I) Experimental paradigm for *in vivo* CNO infusion.
 (J–L) Densities of activated rNSC (nestin⁺EdU⁺) (J), proliferating progenitors and neuroblasts (EdU⁺) (K), and rNSC pool (nestin⁺) (L) (n = 3 for control, and n = 5 for hM4Di).

*p < 0.05 by Student's t test.

Values represent mean \pm SEM. See also Figure S3.

cells (Figures S3C–S3G). *In vivo* suppression of VGAT^{MS-DG} projections led to a significant increase of NSC activation (Figure 3J) without affecting neural progenitors (Figure 3K) or the NSC pool (Figure 3L). These results demonstrated that activity of VGAT^{MS-DG} projections is both necessary and sufficient to regulate rNSC quiescence in the adult DG.

PV Interneurons Are Depolarized by GABA in the Adult DG

GABA, as a classical inhibitory neurotransmitter, would be expected to inhibit dentate PV interneurons and activate rNSCs. Conversely, inhibition of VGAT^{MS-DG} projections would be expected to disinhibit dentate PV interneurons and inhibit rNSCs.

However, our results demonstrated otherwise (Figure 3). This led us to hypothesize instead, that GABA depolarizes dentate PV interneurons. To examine this, we used gramicidin perforated patch to record the chloride gradient of PV interneurons labeled with AAV-DIO-YFP in PV-Cre mice upon focal GABA ejection. At the resting membrane potential (-65.7 ± 4.2 mV), dentate PV interneurons depolarized to focal GABA (Figures 4A and 4B). The depolarizing GABA effect on dentate PV cells was shunting in nature since it was not able to induce action potential firing. Supporting this, the GABA reversal potential in dentate PV interneurons was -50 mV (-48 ± 5.3 mV) under perforated-patch recording in response to electrical stimulation of the SGZ/hilus border (where VGAT^{MS-DG} projections are located) (Figures S4A and S4B).

We further confirmed this depolarizing GABA action by Ca²⁺ imaging. We selectively labeled adult dentate PV interneurons by delivering an AAV-expressing Cre-dependent GCAMP3 (AAV-DIO-GCAMP3) to the DG of PV-Cre mice. Interestingly, we found that adult PV neurons exhibited significant Ca²⁺ in response to GABA_AR agonist muscimol (10 μ M), which was abolished by the Ca²⁺ channel inhibitor La³⁺ (50 μ M) or by the P/Q type Ca²⁺ channel blocker ω -Agatoxin TK (100 nM) (Figures 4C and 4E). In contrast, dentate somatostatin (SST) neurons labeled by AAV-DIO-GCAMP3 using SST-Cre mice (Taniguchi et al., 2011) exhibited decreased Ca²⁺ signals in response to muscimol (Figures 4C–4E). Taken together, these results suggest that GABA depolarizes dentate PV neurons and raises intracellular Ca²⁺, which in turn increases the release probability of the PV terminals apposed to NSCs.

To confirm the role of dentate PV interneurons in mediating MS GABAergic inputs onto rNSCs *in vivo*, we labeled MS GABAergic neurons with Cre-dependent AAV-DIO-hM4Di and DG PV cells with Flp-dependent AAV-fDIO-hM3Dq using VGAT-Cre::PV-FLP double-transgenic mice. Local CNO infusion permitted simultaneous manipulation of MS-DG GABAergic projections and the dentate PV interneurons (Figures 4F, 4G, and S4C–S4E). We validated chemogenetic activation of dentate PV interneurons by slice electrophysiology (Figures S4C–S4E). We then examined the quiescence of NSCs upon simultaneous inhibition of MS-DG GABAergic projections and activation of dentate PV interneurons. Interestingly, we observed a significant decrease of activated NSCs in mice injected with AAV-DIO-hM4Di (MS) and AAV-fDIO-hM3Dq (DG) compared to the control group (AAV-fDIO-YFP in DG) (Figure 4H). While chemogenetic inhibition of MS-DG projections activated NSCs (Figures 3H–3L), concurrent chemogenetic activation of dentate PV neurons abolished this increased NSC activation, thus providing causal evidence that dentate PV interneurons mediate septo-hippocampal GABAergic regulation of rNSCs *in vivo*.

MS PV Projection Neurons Alone Are Not Sufficient to Regulate NSC Quiescence

We sought to further characterize the GABAergic populations in the MS that are responsible for NSC regulation. Rabies tracing data showed that 32% of the MS RV-labeled inputs to dentate PV interneurons were immunopositive for PV (Figures 5A and 5B). Since 56% of total RV-labeled inputs in the MS were GABAergic (Figure 1G), we concluded that there are at least two populations of GABAergic DG projecting neurons in the MS, namely, PV⁺ and PV⁻ populations. As PV neurons were

thought to be the major MS-DG GABAergic projection onto dentate PV interneurons (Kiss et al., 1990; Leranth and Vertes, 1999; Unal et al., 2015), we asked whether the PV⁺ population is sufficient to regulate the quiescence of NSCs. To address this, we injected Cre-dependent YFP or ChR2-YFP to the MS of PV-Cre mice to selectively label PV neurons (Figures 5C and 5D). Consistent with PV neurons only constituting \sim 25% of total GABA neurons in the MS (Figures 5A and 5B), MS PV collaterals were found at much reduced levels compared to VGAT^{MS-DG} projections (Figure 5E). Additionally, the density of MS-PV contacts on the DG-PV somas was markedly reduced compared to MS-VGAT contacts (Figures 5F and S5C). Interestingly, 53% of MS PV cells were transduced by AAV in the PV-Cre mice (Figure 5G) compared to 89% in the VGAT-Cre mice (Figure S5B). This accounts for \sim 60% of MS PV cells labeled in the VGAT-Cre line. However, the number of dentate PV neurons contacted by PV^{MS-DG} collaterals is only \sim 20% of the dentate PV neurons contacted by VGAT^{MS-DG} collaterals (18% in PV-Cre mice versus 91% in VGAT-Cre mice) (Figure 5H). This corroborates the involvement of MS PV⁻ GABA projections in regulating NSCs. Supporting this, optogenetic activation of PV^{MS-DG} projections expressing ChR2-YFP (Figures 5I and 5J) is not sufficient to alter quiescence of NSCs (Figure 5K). Similar to VGAT-Cre mice, activation of PV^{MS-DG} projections did not alter proliferation of neural progenitors (Figure 5L) nor the size of NSC pool (Figure 5M). These results together suggest that MS PV projections alone appear insufficient to regulate NSC quiescence *in vivo*. Interestingly, the *in situ* data available through Allen Brain Atlas exhibited an abundant expression of the LIM homeodomain factor *Lhx6* in the MS (Figure S5D). As *Lhx6* is expressed in cortical PV and SST neurons and is necessary for their differentiation (Kepecs and Fishell, 2014), we injected Cre-dependent AAV-DIO-YFP to the MS of *Lhx6*-Cre mice (Fogarty et al., 2007). Nearly 100% of YFP neurons in the MS of the *Lhx6*-Cre mice were GABA⁺ (Figure S5E). Of these YFP neurons, \sim 40% of them were PV⁺ representing \sim 87% of the total PV neurons in the MS (Figures S5F and S5G). Surprisingly, no YFP neurons were positive for SST (data not shown). Furthermore, we observed prominent MS-DG projections from *Lhx6*-Cre mice injected with AAV-DIO-YFP (Figure S5H), similar to the projection pattern from VGAT-Cre mice. These data suggest the potential involvement of SST⁻, PV⁻ *Lhx6*⁺ GABA projection neurons in regulating NSC quiescence. Furthermore, these neurons may represent distinct GABA neuron population(s) derived from the medial ganglionic eminence (MGE), thus highlighting the regional complexity of interneurons. Future studies using single-cell RNA-sequencing of MS GABAergic input neurons will provide definitive identification of these distinct populations.

Genetic Ablation of MS GABA Neurons Leads to Excessive Stem Cell Activation and Stem Cell Pool Depletion

Precise control of NSC activity is essential for the long-term maintenance of the stem cell pool and sustainable neurogenesis. Manipulating activity of VGAT^{MS-DG} projections over the short-term bi-directionally regulated activation and quiescence states of NSCs. However, the long-term consequences of disrupted activity of VGAT^{MS-DG} projections remain unknown. Typically, rNSCs produce neuronal precursors upon activation followed

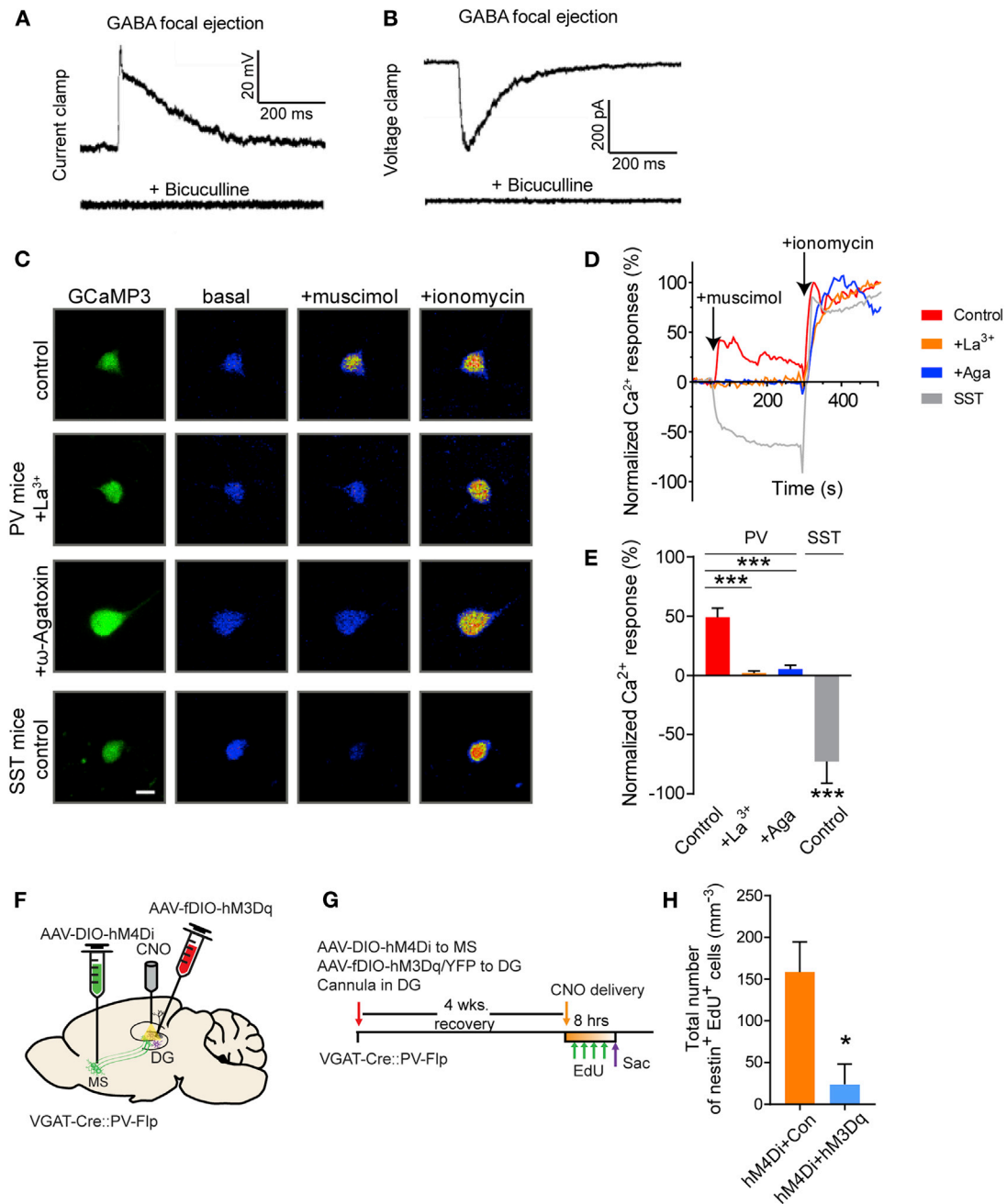


Figure 4. GABA Induces Depolarization and Ca²⁺ Influx in PV Interneurons in the Adult DG

(A and B) Gramicidin-perforated patch-clamp recordings of dentate PV neurons in response to GABA focal ejection (5 μ M) with or without bicuculline (50 μ M) under the current-clamp (A) and voltage-clamp (B) mode ($n = 6$).

(C–E) Ca²⁺ imaging analysis of neuronal responses to GABA_AR agonist muscimol (10 μ M) and Ca²⁺ ionophore ionomycin (10 μ M). Adult PV or SST neurons were labeled with AAV-expressing GCaMP3 in PV-Cre or SST-Cre mice. (C) Confocal images of Ca²⁺ responses without or with pre-treatment of La³⁺ (50 μ M) or ω -Agatoxin TK (100 nM). Scale bar, 20 μ m. (D) Calcium time-course analysis. (E) Summary of the mean peak Ca²⁺ responses. Values are normalized to the mean fluorescence intensity at baseline (0%) and after ionomycin (100%) ($n = 7$ cells from >3 mice for each group).

(F) Viral injection and DG cannulation scheme in VGAT-Cre::PV-Flp mice.

(G) Experimental paradigm for *in vivo* CNO infusion.

(H) Density of activated rNSC (nestin⁺EdU⁺) ($n = 5$ for hM4Di+Con, and $n = 4$ for hM4Di+hM3Dq).

* $p < 0.05$, *** $p < 0.001$ by Student's *t* test.

Values represent mean \pm SEM. See also Figure S4.

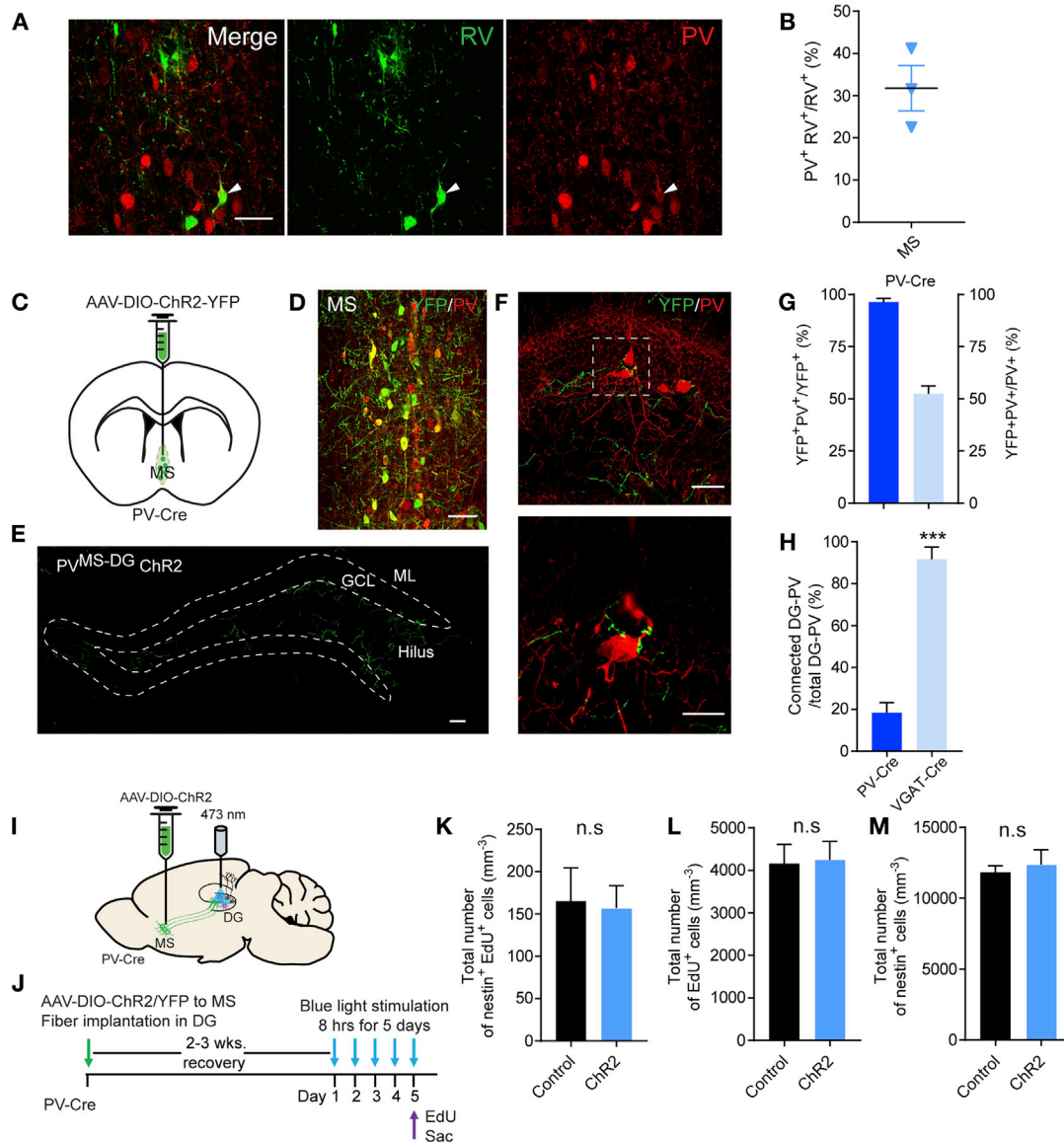


Figure 5. MS PV Projection Neurons Alone Are Not Sufficient to Regulate NSC Quiescence

(A) Confocal images showing RV input neurons in the MS colocalize with PV marker. Arrowheads pointing to PV⁺ RV⁺ cells. Scale bar, 50 μ m.

(B) Percentage of PV⁺ RV⁺ out of total RV input cells in the MS (n = 3).

(C) AAV-DIO-YFP injection scheme to the MS of PV-Cre mice.

(D) Composite confocal image showing selective targeting of MS PV neurons through stereotaxic delivery of AAV-DIO-YFP to PV-Cre mice. Scale bar, 50 μ m.

(E) Composite confocal image of sparse AAV-DIO-YFP-labeled MS PV projections to the SGZ and hilus. Scale bar, 50 μ m.

(F) Axonal collaterals from MS PV cells are closely associated with the soma of dentate PV interneurons. Scale bar, 50 μ m (top) and 20 μ m (bottom).

(G) YFP viral labeled MS PV neurons in PV-Cre mice (n = 6).

(H) Connected percentage of MS projections to DG-PV neurons (n = 6 for PV-Cre, and n = 4 for VGAT-Cre).

(I) AAV-DIO-ChR2-YFP injection scheme to the MS in VGAT-Cre mice.

(J) Experimental paradigm for *in vivo* optogenetic stimulation.

(K–M) Density of activated rNSC (nestin⁺Edu⁺) (K), proliferating cells (Edu⁺) (L), and the rNSC pool (nestin⁺) (M) (n = 5 for control and n = 6 for Chr2).

***p < 0.001 by Student's t test.

Values represent mean \pm SEM. See also Figure S5.

by differentiation into astrocytes, resulting in a progressive depletion of the NSC pool (Encinas et al., 2011). To chronically manipulate activity of VGAT^{MS-DG} projections, we ablated MS GABA neurons and their projections by introducing Cre-depend

ent AAV-expressing taCasp3-2A-TEVp (AAV-FLEX-taCasp3-TEVp) to the MS of the adult VGAT-Cre mice (Yang et al., 2013) (Figures 6A and 6B). By 6 weeks following AAV injection, MS GABAergic neurons were successfully ablated compared

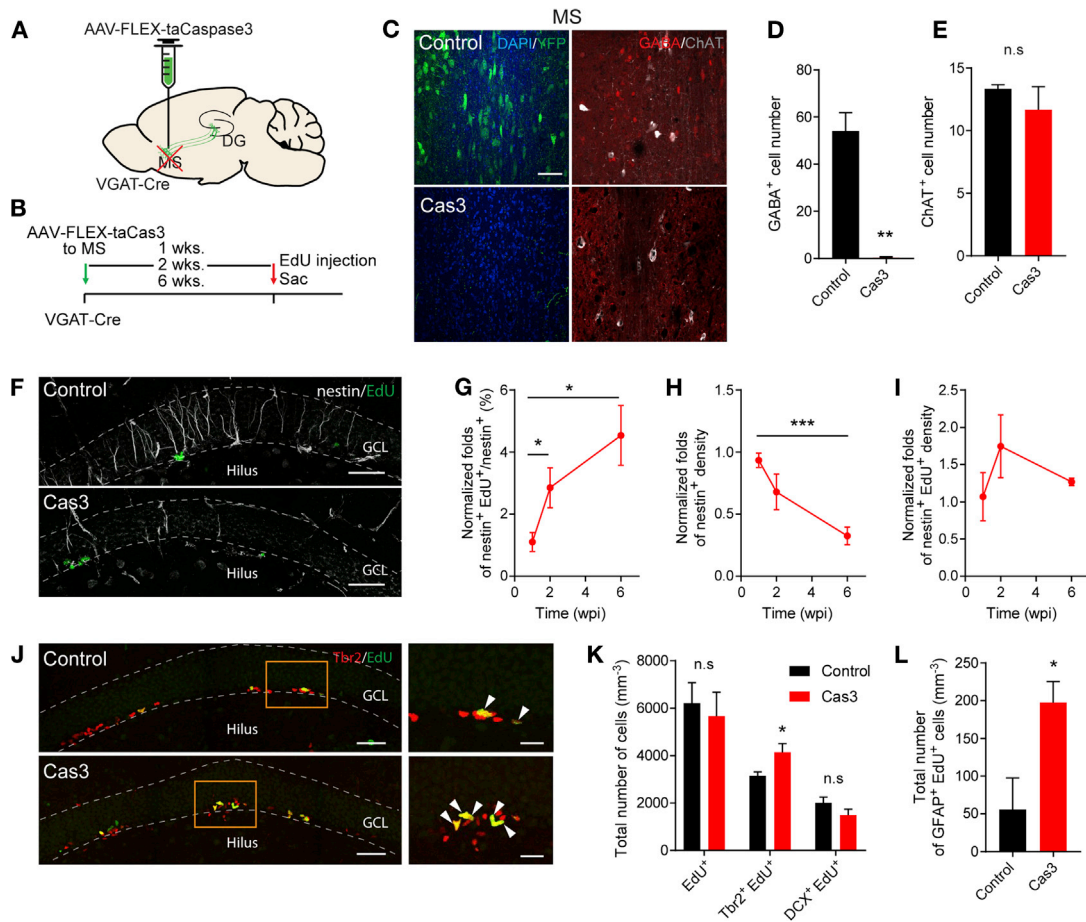


Figure 6. Genetic Ablation of MS GABA Neurons Leads to Excessive Stem Cell Activation and Stem Cell Pool Depletion

(A) AAV-DIO-YFP or AAV-Flex-taCaspase3 injection scheme into the MS of adult VGAT-Cre mice.

(B) Experimental scheme of chronic ablation of MS GABAergic neurons in VGAT-Cre mice.

(C) Composite confocal images showing selective ablation of GABAergic neurons in the MS 6 weeks after AAV injection. Scale bar, 50 μ m.

(D) Number of GABAergic neurons in the MS ($n = 3$ for control and caspase).

(E) Number of ChAT neurons in the MS ($n = 3$ for control and caspase).

(F) Confocal images of the nestin⁺ and EdU⁺ cells in the DG from control and caspase conditions at 6 wpi. Scale bar, 50 μ m.

(G–I) rNSC activation and rNSC pool at 1, 2, and 6 wpi. Data are normalized to control. (G) Normalized fold change in percentage of rNSC activation (H) nestin⁺ rNSC pool and (I) activated NSCs (nestin⁺EdU⁺) (1 and 2 wpi: $n = 4$ for control and caspase. 6 wpi: $n = 5$ for control, and $n = 4$ for caspase).

(J) Composite confocal images of Tbr2 and EdU⁺ cells in the DG for the control and caspase conditions at 6 wpi. Scale bar, 50 μ m.

(K) Density of proliferating cells (EdU⁺), proliferating progenitors (Tbr2⁺EdU⁺), and mitotic neuroblasts (DCX⁺EdU⁺) at 6 wpi ($n = 4$ for control and caspase).

(L) Density of differentiating astrocytes (GFAP⁺EdU⁺) ($n = 4$ for control and caspase).

* $p < 0.05$, ** $p < 0.01$, *** $p < 0.001$ by Student's *t* test.

Values represent mean \pm SEM. See also Figure S6.

to controls (AAV-DIO-YFP) (Figures 6C and 6D). In contrast, ChAT-expressing neurons remained unaffected (Figure 6E), confirming specificity of the caspase system in ablating MS GABA neurons. Additionally, a mixture of AAV-DIO-YFP and AAV-DIO-caspase at a ratio of 1:1, efficiently revealed ablated VGAT^{MS-DG} projections in the SGZ and hilus (Figure S6).

We then examined NSC activation and the NSC pool size at 1, 2, and 6 weeks following ablation of MS GABA neurons. We found that the activated fraction of NSCs was significantly increased 2 weeks following ablation and continued to increase at 6 weeks following ablation (Figures 6F and 6G). Furthermore, excessive activation was accompanied by a reduction of the NSC pool starting from 2 weeks following ablation and reaching

significance by 6 weeks (Figure 6H). The density of activated NSCs (nestin⁺ EdU⁺) was not significantly altered (Figure 6I), suggesting that increased NSC activation was a result of a reduced NSC pool. Lineage tracing studies have shown that quiescent NSCs can give rise to highly proliferative Tbr2 intermediate progenitors. We examined the number of proliferating progenitors (Tbr2⁺ EdU⁺) at 6 weeks following ablation. Consistent with increased activation of NSCs, we observed a significant increase in the number of Tbr2⁺ EdU⁺ proliferating progenitors without altering the number of DCX⁺ EdU⁺ neuroblasts (Figures 6J and 6K). These results suggest that loss of MS-DG GABAergic projections led to increased neuronal differentiation of NSCs. Neuronal differentiation is often accompanied by astrocytic

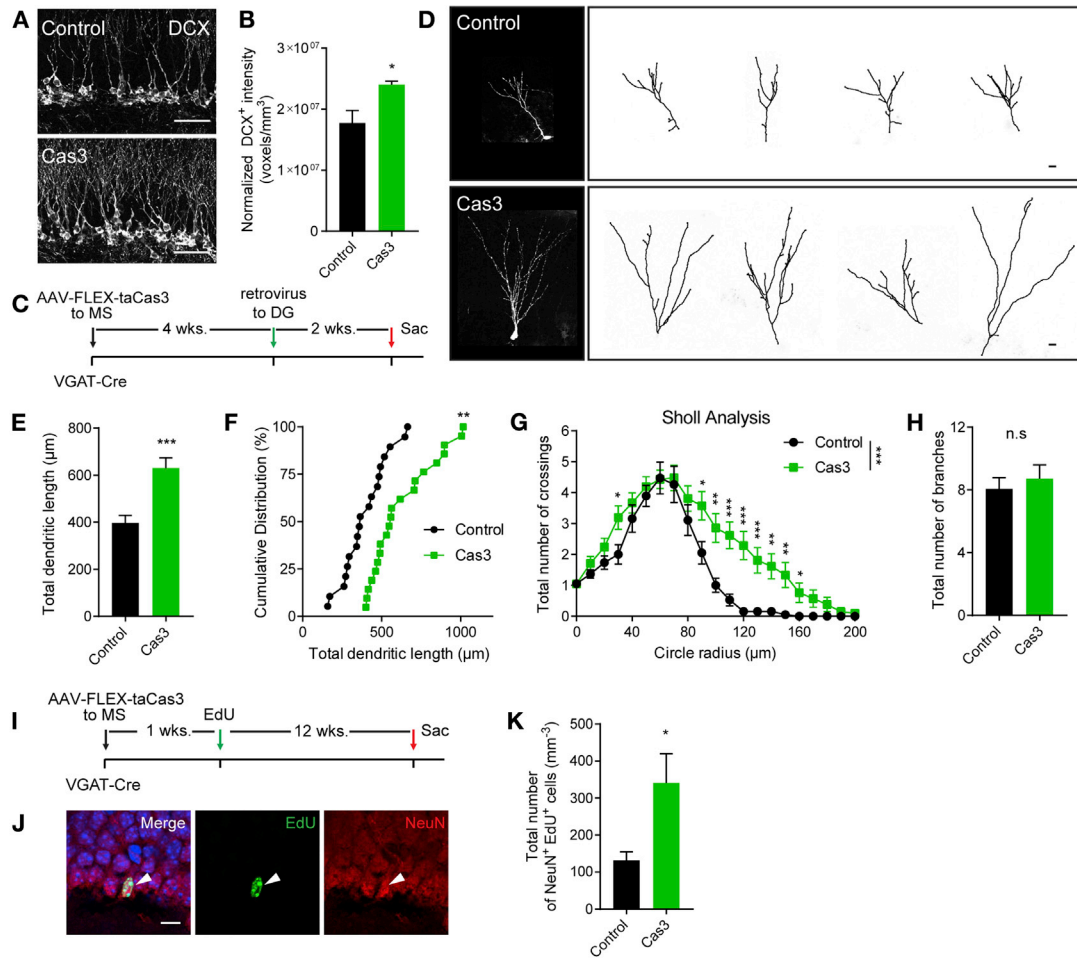


Figure 7. Chronic Ablation of MS GABA Neurons Leads to Impaired Hippocampal Neurogenesis

- (A) Composite confocal images showing DCX cells in the DG in control and caspase conditions at 6 wpi. Scale bar, 50 μm .
 (B) Density of normalized fluorescence intensity of DCX immature neurons ($n = 4$ for control and caspase).
 (C) Experimental scheme of chronic ablation of MS GABAergic neurons and retroviral birth-dating of adult born neurons in VGAT-Cre mice.
 (D) Representative dendritic trees of GFP⁺ newborn neurons. Scale bar, 10 μm .
 (E) Total dendritic length ($n = 20$ cells from 4 mice for both control and caspase).
 (F) Cumulative distribution of total dendritic length (same dataset from E). ** $p < 0.01$ by Kolmogorov-Smirnov test.
 (G) Sholl analysis of GFP⁺ newborn neurons at 14 dpi (same dataset from E).
 (H) Total number of dendritic branches (same dataset from E).
 (I) Experimental scheme of chronic ablation of MS GABAergic neurons in VGAT-Cre mice.
 (J) Confocal images of mature neurons (NeuN⁺EdU⁺) following 13 weeks of MS GABA neuron ablation. Scale bar, 10 μm .
 (K) Density of mature neurons (NeuN⁺EdU⁺) ($n = 4$ for control and caspase).

* $p < 0.05$, ** $p < 0.01$, *** $p < 0.001$ by Student's *t* test.
 Values represent mean \pm SEM. See also Figure S7.

differentiation (Encinas et al., 2011). Consistent with this, we observed a significant increase in activated astrocytes (Figure 6L). Together, these data suggest that chronic ablation of VGAT^{MS-DG} projections led to excessive NSC activation that in turn induced increased NSC differentiation and pool depletion.

Chronic Ablation of MS GABA Neurons Leads to Impaired Hippocampal Neurogenesis

We sought to investigate whether the depletion of NSCs is accompanied by impaired hippocampal neurogenesis. A reduced NSC pool is normally associated with a transient

activation of quiescent NSCs and an increase in proliferating progenitors, which in turn transiently increases production of immature and mature neurons. We first examined the density of DCX immature neurons by quantifying DCX immunofluorescence (voxels/ mm^3) across the whole DG, which provided an overall readout of the density of immature neurons (Ingle et al., 2013). We found a significant increase in the intensity of DCX immunofluorescence in the caspase group at 6 weeks following ablation (Figures 7A and 7B). Additionally, we examined dendritic development of immature neurons upon chronic ablation of MS GABA neurons. We took a retroviral-based approach to birth-date newborn neurons generated during chronic ablation

of MS GABA neurons and examined dendritic development in immature neurons at 14 days post-retroviral expression (Figure 7C). Interestingly, we observed a significant increase in dendritic length and crossings in the caspase group compared to controls (Figures 7D–7G) without significant change in branch number (Figure 7H). These data suggest that not only is the number of immature neurons significantly altered upon chronic ablation of MS GABA neurons, but the morphology of new neurons generated under this aberrant environment was also significantly different from the controls.

Finally, we examined the production of mature neurons upon chronic ablation of MS GABA neurons. We injected Cre-dependent AAV-expressing taCasp3-2A-TEVp to the MS of the VGAT-Cre mice, and 1 week after injection we labeled the starting population of proliferating cells with 4 EdU injections. Three months later, we examined the number of mature neuron population (NeuN⁺EdU⁺) (Figure 7I) and observed a significant increase in the number of the NeuN⁺EdU⁺ cells (Figures 7J and 7K). These data suggest that chronic ablation of MS GABA neurons led to increased survival of newborn neurons.

DISCUSSION

The continuous generation of new neurons in the DG is a prominent example of structural plasticity in the adult mammalian brain and is a process highly regulated by neural network activity. Consistent with the notion that adult neurogenesis has a dynamic set point, the MS-DG GABAergic network displayed bi-directional control of *in vivo* NSC behaviors. This inhibitory network includes MS GABAergic neurons and DG GABA-depolarizing PV interneurons to couple global brain activity to the neurogenic niche (Figure S7A). Our findings have a number of implications on dynamic control of adult hippocampal neurogenesis and on developing strategies in treating brain disorders arising from aberrant hippocampal neurogenesis, such as Alzheimer's disease and schizophrenia.

Our recent studies identified DG PV interneurons as a unique local niche component that regulates quiescence of NSCs and NSC pool maintenance through tonic GABA signaling (Song et al., 2012b). Those results highlighted the critical roles of specific local interneuron populations in controlling adult NSCs and hippocampal neurogenesis. Our current results further demonstrate that neuronal network activity mediated by long-range MS GABAergic neurons are both necessary and sufficient to regulate adult NSCs and hippocampal neurogenesis through local PV interneurons. Therefore, local PV interneurons may serve as a “hub” capable of relaying outside information to NSCs through their distal inputs. Using RV-based monosynaptic retrograde tracing, we found that the major distal inputs to local PV interneurons are restricted within the MS and DB; thus, these brain regions are in an ideal position to relay various physiological or pathological stimuli to the neurogenic niche and impact hippocampal neurogenesis. Indeed, the MS and DB complex is part of the forebrain, which has been shown to receive inputs from a wide distribution of brain areas across the cerebral nuclei, cerebral cortex, and brain stem, including nucleus accumbens, lateral hypothalamus, central nucleus of the amygdala, raphe, and many others (Do et al., 2016). Moreover, our rabies tracing identified GABAergic neurons in the MS as the major inputs to

the dentate PV interneurons; thus, MS GABAergic neurons may receive direct inputs from distal brain regions to regulate NSCs through dentate PV interneurons. This provides a plausible explanation for why adult hippocampal neurogenesis is particularly sensitive to physiological and pathological conditions (Kempermann, 2015; Piatti et al., 2011; Song et al., 2012a, 2016).

We also identified a GABA-depolarizing property of local PV interneurons that has a profound impact on the NSC pool and hippocampal neurogenesis in the adult brain. Given that NSCs do not have functional synapses (Tozuka et al., 2005), NSCs likely sense GABA spillover from nearby PV synapses onto mature granule cells (Song et al., 2012b). Strikingly, PV neurons in the adult DG exhibit depolarization and Ca²⁺ influx in response to GABA, which is in sharp contrast to most mature neurons that are hyperpolarized by GABA (Ben-Ari, 2002; Owens and Kriegstein, 2002). The GABA depolarizing property is supported by a recent study that modeled action potential thresholds for fast-spiking cells at –40.5 mV (Song et al., 2011). Because GABA shunts PV neurons, it is the temporal and spatial integration of depolarizations and shunting that ultimately determine the release probability of GABA from dentate PV neurons. Notably, synapses formed onto PV interneurons are highly efficient, as GABA release can be induced with activation of three or fewer Ca²⁺ channels (Bucurenciu et al., 2010). Interestingly, sources of GABA signaling onto dentate PV cells may come from heterogeneous MS GABAergic projection neurons, including both PV⁺ and PV[–] populations. We speculate that MS PV⁺ and PV[–] GABAergic neurons may need to coordinate their depolarizing GABA activity onto dentate PV interneurons to collectively regulate NSCs. Future investigations on molecular profiles and electrophysiological properties of distinct MS GABAergic populations will provide valuable information on how distinct GABAergic networks regulate adult NSCs and hippocampal neurogenesis.

A recent study showed that kainic-acid-induced epileptiform activity led to stem cell pool depletion (Sierra et al., 2015). It is possible that ablation of VGAT^{MS-DG} projections also leads to disinhibition of mature granule cells and epileptiform activity in the adult DG. However, we did not observe any seizure or epileptiform activity in the caspase mice (Figure S7B), measured by 48 hr of continuous time-locked intrahippocampal video EEG recording. This suggests that seizure or epileptiform activity is not required for our observed NSC pool depletion. Lack of epileptiform activity does not rule out whether subtle hyperactivity exists due to an excitation and inhibition imbalance. We have indeed noticed that the threshold for flurothyl-induced seizure was reduced in caspase mice (Figures S7C–S7E), suggesting a subtle chronic network hyperexcitability could lead to NSC pool depletion and impaired hippocampal neurogenesis.

MS GABAergic neurons have been shown to play a critical role in regulating hippocampal theta rhythm (Hangya et al., 2009), an electrophysiological characteristic essential for hippocampal-dependent learning and memory (Düzel et al., 2010). Interestingly, activation of VGAT^{MS-DG} projections in the theta frequency range (Mann and Paulsen, 2007) is effective in maintaining the quiescence of NSCs. These results suggest that active engagement of both MS and the hippocampus during periods of exploration or learning may be critical for maintaining NSCs. Many physiological stimuli, such as exploration of novel environments, aging, or pathological conditions such as neurodegenerative

diseases, affect the MS-DG GABAergic network. For instance, in a triple transgenic mouse model of Alzheimer's disease (AD), selective loss of MS GABAergic (but not ChAT) neurons and dentate interneurons (including PV neurons) were observed (Loreth et al., 2012). Furthermore, these mice displayed an aberrant initial increase in neurogenesis followed by a decrease of adult hippocampal neurogenesis at the later stage (Kuhn et al., 2007; Lazarov and Marr, 2010). These data suggest that disruption of GABAergic neurons in the MS and DG correlates with impaired adult hippocampal neurogenesis under pathological conditions. Substantial evidence suggests that newborn neurons participate in specific brain functions, including learning and memory, stress responses, and mood regulation, while aberrant adult neurogenesis contributes to neurological and mental disorders. Therefore, targeting the MS-DG GABAergic circuit may constitute a therapeutic strategy to combat hippocampal hyperexcitability associated with various neurological disorders in order to preserve the NSC pool, maintain sustainable and healthy hippocampal neurogenesis, and promote cognitive functions.

STAR★METHODS

Detailed methods are provided in the online version of this paper and include the following:

- KEY RESOURCES TABLE
- CONTACT FOR REAGENT AND RESOURCE SHARING
- EXPERIMENTAL MODEL AND SUBJECT DETAILS
- METHOD DETAILS
 - Stereotaxic surgery
 - Immunohistochemistry
 - Imaging
 - Slice Electrophysiology
 - Ca²⁺ imaging
 - Time-locked video-EEG recording
 - Flurothyl-induced seizure
- QUANTIFICATION AND STATISTICAL ANALYSIS
 - General
 - Cell quantification
 - Slice Electrophysiology
 - Ca²⁺ imaging
- DATA AND SOFTWARE AVAILABILITY

SUPPLEMENTAL INFORMATION

Supplemental Information includes seven figures and can be found with this article online at <https://doi.org/10.1016/j.stem.2017.10.003>.

AUTHOR CONTRIBUTIONS

J.S. led the project, designed and supervised experiments, and wrote the manuscript; H.B. designed experiments and performed surgeries and imaging analysis; B.A. performed electrophysiology recordings; W.L. provided partial financial support for H.B.; B.G. and B.P. performed in vivo EEG recording; Z.W. performed calcium imaging; S.-A.L. and I.H. assisted with experiments; and C.R. and K.D. provided Flp-dependent AAV-hM3Dq.

ACKNOWLEDGMENTS

We thank Dr. Bryan Roth, Dr. Garret Stuber, and members of the Song lab for comments and discussions; Dr. Jenny Hsieh from Southwestern Medical

Center for retrovirus; and Dipendra Aryal from the Roth lab for technical support of CNO local infusion. This work was supported by grants awarded to J.S. from NARSAD, American Heart Association (14SDG20440029), Whitehall Foundation, and NIH (R01MH111773 and R21MH106939). H.B. was partially supported by National Major Scientific Instruments Development Project (2012YQ03026007) and National Nature Science Foundation of China (81421061).

Received: January 23, 2017
 Revised: August 28, 2017
 Accepted: October 12, 2017
 Published: November 2, 2017

REFERENCES

- Armstrong, C., and Soltesz, I. (2012). Basket cell dichotomy in microcircuit function. *J. Physiol.* 590, 683–694.
- Atasoy, D., Aponte, Y., Su, H.H., and Sternson, S.M. (2008). A FLEX switch targets Channelrhodopsin-2 to multiple cell types for imaging and long-range circuit mapping. *J. Neurosci.* 28, 7025–7030.
- Ben-Ari, Y. (2002). Excitatory actions of gaba during development: The nature of the nurture. *Nat. Rev. Neurosci.* 3, 728–739.
- Bucurenciu, I., Bischofberger, J., and Jonas, P. (2010). A small number of open Ca²⁺ channels trigger transmitter release at a central GABAergic synapse. *Nat. Neurosci.* 13, 19–21.
- Cardin, J.A., Carlén, M., Meletis, K., Knoblich, U., Zhang, F., Deisseroth, K., Tsai, L.H., and Moore, C.I. (2009). Driving fast-spiking cells induces gamma rhythm and controls sensory responses. *Nature* 459, 663–667.
- Do, J.P., Xu, M., Lee, S.H., Chang, W.C., Zhang, S., Chung, S., Yung, T.J., Fan, J.L., Miyamichi, K., Luo, L., et al. (2016). Cell type-specific long-range connections of basal forebrain circuit. *eLife*. Published online: September 19, 2016. <https://doi.org/10.7554/eLife>.
- Düzel, E., Penny, W.D., and Burgess, N. (2010). Brain oscillations and memory. *Curr. Opin. Neurobiol.* 20, 143–149.
- Encinas, J.M., Michurina, T.V., Peunova, N., Park, J.H., Tordo, J., Peterson, D.A., Fishell, G., Koulakov, A., and Enikolopov, G. (2011). Division-coupled astrocytic differentiation and age-related depletion of neural stem cells in the adult hippocampus. *Cell Stem Cell* 8, 566–579.
- Fogarty, M., Grist, M., Gelman, D., Marín, O., Pachnis, V., and Kessaris, N. (2007). Spatial genetic patterning of the embryonic neuroepithelium generates GABAergic interneuron diversity in the adult cortex. *J. Neurosci.* 27, 10935–10946.
- Freund, T.F., and Antal, M. (1988). GABA-containing neurons in the septum control inhibitory interneurons in the hippocampus. *Nature* 336, 170–173.
- Hangya, B., Borhegyi, Z., Szilágyi, N., Freund, T.F., and Varga, V. (2009). GABAergic neurons of the medial septum lead the hippocampal network during theta activity. *J. Neurosci.* 29, 8094–8102.
- Harrison, P.J. (2004). The hippocampus in schizophrenia: A review of the neuropathological evidence and its pathophysiological implications. *Psychopharmacology (Berl.)* 174, 151–162.
- Hefft, S., and Jonas, P. (2005). Asynchronous GABA release generates long-lasting inhibition at a hippocampal interneuron-principal neuron synapse. *Nat. Neurosci.* 8, 1319–1328.
- Ingle, N.P., Xue, L., and Reineke, T.M. (2013). Spatiotemporal cellular imaging of polymer-pDNA nanocomplexes affords in situ morphology and trafficking trends. *Mol. Pharm.* 10, 4120–4135.
- Kempermann, G. (2015). Activity dependency and aging in the regulation of adult neurogenesis. *Cold Spring Harb. Perspect. Biol.* Published online November 2, 2015. <https://doi.org/10.1101/cshperspect.a018929>.
- Kempermann, G., Krebs, J., and Fabel, K. (2008). The contribution of failing adult hippocampal neurogenesis to psychiatric disorders. *Curr. Opin. Psychiatry* 21, 290–295.
- Kepecs, A., and Fishell, G. (2014). Interneuron cell types are fit to function. *Nature* 505, 318–326.

- Kim, J.Y., Duan, X., Liu, C.Y., Jang, M.H., Guo, J.U., Pow-anpongkul, N., Kang, E., Song, H., and Ming, G.L. (2009). DISC1 regulates new neuron development in the adult brain via modulation of AKT-mTOR signaling through KIAA1212. *Neuron* 63, 761–773.
- Kiss, J., Patel, A.J., and Freund, T.F. (1990). Distribution of septohippocampal neurons containing parvalbumin or choline acetyltransferase in the rat brain. *J. Comp. Neurol.* 298, 362–372.
- Kohara, K., Pignatelli, M., Rivest, A.J., Jung, H.Y., Kitamura, T., Suh, J., Frank, D., Kajikawa, K., Mise, N., Obata, Y., et al. (2014). Cell type-specific genetic and optogenetic tools reveal hippocampal CA2 circuits. *Nat. Neurosci.* 17, 269–279.
- Kriegstein, A., and Alvarez-Buylla, A. (2009). The glial nature of embryonic and adult neural stem cells. *Annu. Rev. Neurosci.* 32, 149–184.
- Kuhn, H.G., Cooper-Kuhn, C.M., Boekhoorn, K., and Lucassen, P.J. (2007). Changes in neurogenesis in dementia and Alzheimer mouse models: Are they functionally relevant? *Eur. Arch. Psychiatry Clin. Neurosci.* 257, 281–289.
- Lazarov, O., and Marr, R.A. (2010). Neurogenesis and Alzheimer's disease: At the crossroads. *Exp. Neurol.* 223, 267–281.
- Le Strat, Y., Ramoz, N., and Gorwood, P. (2009). The role of genes involved in neuroplasticity and neurogenesis in the observation of a gene-environment interaction (GxE) in schizophrenia. *Curr. Mol. Med.* 9, 506–518.
- Lein, E.S., Hawrylycz, M.J., Ao, N., Ayres, M., Bensinger, A., Bernard, A., Boe, A.F., Boguski, M.S., Brockway, K.S., Byrnes, E.J., et al. (2007). Genome-wide atlas of gene expression in the adult mouse brain. *Nature* 445, 168–176.
- Leranth, C., and Vertes, R.P. (1999). Median raphe serotonergic innervation of medial septum/diagonal band of Broca (MSDB) parvalbumin-containing neurons: Possible involvement of the MSDB in the desynchronization of the hippocampal EEG. *J. Comp. Neurol.* 410, 586–598.
- Loreth, D., Ozmen, L., Revel, F.G., Knoflach, F., Wetzel, P., Frotscher, M., Metzger, F., and Kretz, O. (2012). Selective degeneration of septal and hippocampal GABAergic neurons in a mouse model of amyloidosis and tauopathy. *Neurobiol. Dis.* 47, 1–12.
- Mann, E.O., and Paulsen, O. (2007). Role of GABAergic inhibition in hippocampal network oscillations. *Trends Neurosci.* 30, 343–349.
- Ming, G.L., and Song, H. (2011). Adult neurogenesis in the mammalian brain: Significant answers and significant questions. *Neuron* 70, 687–702.
- Miyamichi, K., Amat, F., Moussavi, F., Wang, C., Wickersham, I., Wall, N.R., Taniguchi, H., Tasic, B., Huang, Z.J., He, Z., et al. (2011). Cortical representations of olfactory input by trans-synaptic tracing. *Nature* 472, 191–196.
- Moss, J., and Toni, N. (2013). A circuit-based gatekeeper for adult neural stem cell proliferation: Parvalbumin-expressing interneurons of the dentate gyrus control the activation and proliferation of quiescent adult neural stem cells. *BioEssays* 35, 28–33.
- Otmakhov, N., Khibnik, L., Otmakhova, N., Carpenter, S., Riahi, S., Asrican, B., and Lisman, J. (2004). Forskolin-induced LTP in the CA1 hippocampal region is NMDA receptor dependent. *J. Neurophysiol.* 91, 1955–1962.
- Overstreet, L.S., and Westbrook, G.L. (2001). Paradoxical reduction of synaptic inhibition by vigabatrin. *J. Neurophysiol.* 86, 596–603.
- Owens, D.F., and Kriegstein, A.R. (2002). Is there more to GABA than synaptic inhibition? *Nat. Rev. Neurosci.* 3, 715–727.
- Paxinos, G., and Franklin, K. (2001). *The Mouse Brain in Stereotaxic Coordinates* (Academic Press).
- Peteanu, L., Huber, D., Sobczyk, A., and Svoboda, K. (2007). Channelrhodopsin-2-assisted circuit mapping of long-range callosal projections. *Nat. Neurosci.* 10, 663–668.
- Piatti, V.C., Davies-Sala, M.G., Espósito, M.S., Mongiat, L.A., Trincherio, M.F., and Schinder, A.F. (2011). The timing for neuronal maturation in the adult hippocampus is modulated by local network activity. *J. Neurosci.* 31, 7715–7728.
- Schindelin, J., Arganda-Carreras, I., Frise, E., Kaynig, V., Longair, M., Pietzsch, T., Preibisch, S., Rueden, C., Saalfeld, S., Schmid, B., et al. (2012). Fiji: An open-source platform for biological-image analysis. *Nat. Methods* 9, 676–682.
- Sierra, A., Martín-Suárez, S., Valcárcel-Martín, R., Pascual-Brazo, J., Aelvoet, S.A., Abiega, O., Deudero, J.J., Brewster, A.L., Bernales, I., Anderson, A.E., et al. (2015). Neuronal hyperactivity accelerates depletion of neural stem cells and impairs hippocampal neurogenesis. *Cell Stem Cell* 16, 488–503.
- Sohal, V.S., Zhang, F., Yizhar, O., and Deisseroth, K. (2009). Parvalbumin neurons and gamma rhythms enhance cortical circuit performance. *Nature* 459, 698–702.
- Song, I., Savtchenko, L., and Semyanov, A. (2011). Tonic excitation or inhibition is set by GABA(A) conductance in hippocampal interneurons. *Nat. Commun.* 2, 376.
- Song, J., Christian, K.M., Ming, G.L., and Song, H. (2012a). Modification of hippocampal circuitry by adult neurogenesis. *Dev. Neurobiol.* 72, 1032–1043.
- Song, J., Zhong, C., Bonaguidi, M.A., Sun, G.J., Hsu, D., Gu, Y., Meletis, K., Huang, Z.J., Ge, S., Enikolopov, G., et al. (2012b). Neuronal circuitry mechanism regulating adult quiescent neural stem-cell fate decision. *Nature* 489, 150–154.
- Song, J., Sun, J., Moss, J., Wen, Z., Sun, G.J., Hsu, D., Zhong, C., Davoudi, H., Christian, K.M., Toni, N., et al. (2013). Parvalbumin interneurons mediate neuronal circuitry-neurogenesis coupling in the adult hippocampus. *Nat. Neurosci.* 16, 1728–1730.
- Song, J., Olsen, R.H., Sun, J., Ming, G.L., and Song, H. (2016). Neuronal circuitry mechanisms regulating adult mammalian neurogenesis. *Cold Spring Harb. Perspect. Biol.* Published online August 1, 2016. <https://doi.org/10.1101/cshperspect.a018937>.
- Taniguchi, H., He, M., Wu, P., Kim, S., Paik, R., Sugino, K., Kvitsiani, D., Fu, Y., Lu, J., Lin, Y., et al. (2011). A resource of Cre driver lines for genetic targeting of GABAergic neurons in cerebral cortex. *Neuron* 71, 995–1013.
- Tian, L., Hires, S.A., Mao, T., Huber, D., Chiappe, M.E., Chalasani, S.H., Petreanu, L., Akerboom, J., McKinney, S.A., Schreier, E.R., et al. (2009). Imaging neural activity in worms, flies and mice with improved GCaMP calcium indicators. *Nat. Methods* 6, 875–881.
- Ting, J.T., Daigle, T.L., Chen, Q., and Feng, G. (2014). Acute brain slice methods for adult and aging animals: Application of targeted patch clamp analysis and optogenetics. *Methods Mol. Biol.* 1183, 221–242.
- Tozuka, Y., Fukuda, S., Namba, T., Seki, T., and Hisatsune, T. (2005). GABAergic excitation promotes neuronal differentiation in adult hippocampal progenitor cells. *Neuron* 47, 803–815.
- Unal, G., Joshi, A., Viney, T.J., Kis, V., and Somogyi, P. (2015). Synaptic targets of medial septal projections in the hippocampus and extrahippocampal cortices of the mouse. *J. Neurosci.* 35, 15812–15826.
- Vong, L., Ye, C., Yang, Z., Choi, B., Chua, S., Jr., and Lowell, B.B. (2011). Leptin action on GABAergic neurons prevents obesity and reduces inhibitory tone to POMC neurons. *Neuron* 71, 142–154.
- Wall, N.R., De La Parra, M., Callaway, E.M., and Kreitzer, A.C. (2013). Differential innervation of direct- and indirect-pathway striatal projection neurons. *Neuron* 79, 347–360.
- Watabe-Uchida, M., Zhu, L., Ogawa, S.K., Vamanrao, A., and Uchida, N. (2012). Whole-brain mapping of direct inputs to midbrain dopamine neurons. *Neuron* 74, 858–873.
- Weissbourd, B., Ren, J., DeLoach, K.E., Guenther, C.J., Miyamichi, K., and Luo, L. (2014). Presynaptic partners of dorsal raphe serotonergic and GABAergic neurons. *Neuron* 83, 645–662.
- Wickersham, I.R., Lyon, D.C., Barnard, R.J., Mori, T., Finke, S., Conzelmann, K.K., Young, J.A., and Callaway, E.M. (2007). Monosynaptic restriction of transsynaptic tracing from single, genetically targeted neurons. *Neuron* 53, 639–647.
- Wilson, R.I., Kunos, G., and Nicoll, R.A. (2001). Presynaptic specificity of endocannabinoid signaling in the hippocampus. *Neuron* 31, 453–462.
- Winkle, C.C., Olsen, R.H., Kim, H., Moy, S.S., Song, J., and Gupton, S.L. (2016). Trim9 deletion alters the morphogenesis of developing and adult-born

hippocampal neurons and impairs spatial learning and memory. *J. Neurosci.* 36, 4940–4958.

Yang, C.F., Chiang, M.C., Gray, D.C., Prabhakaran, M., Alvarado, M., Juntti, S.A., Unger, E.K., Wells, J.A., and Shah, N.M. (2013). Sexually dimorphic neurons in the ventromedial hypothalamus govern mating in both sexes and aggression in males. *Cell* 153, 896–909.

Zhao, C., Deng, W., and Gage, F.H. (2008). Mechanisms and functional implications of adult neurogenesis. *Cell* 132, 645–660.

Zhou, M., Li, W., Huang, S., Song, J., Kim, J.Y., Tian, X., Kang, E., Sano, Y., Liu, C., Balaji, J., et al. (2013). mTOR Inhibition ameliorates cognitive and affective deficits caused by *Disc1* knockdown in adult-born dentate granule neurons. *Neuron* 77, 647–654.

STAR★METHODS

KEY RESOURCES TABLE

REAGENT or RESOURCE	SOURCE	IDENTIFIER
Antibodies		
Anti-Goat GFP	Rockland	Cat# 600-101-215; RRID: AB_218182
Anti-Rabbit GABA	Sigma	Cat# A2052-100UL
Anti-Rabbit/Mouse PV	Swant	Cat# PV27/235
Anti-Mouse Calretinin	Swant	Cat# 6B3
Anti-Rabbit nNos	Life Tech	Cat# 617000; RRID: AB_88207
Anti-Rat mCherry	Life Tech	Cat# M11217; RRID: AB_2536611
Anti-Chicken Nestin	Aves	Cat# NES; RRID: AB_2314882
Anti-Goat DCX	Santa Cruz	Cat# SC-8066; RRID: AB_2088494
Anti-Mouse Syn1	Synaptic Systems	Cat# 106 011; RRID: AB_993029
Anti-Goat ChAT	Millipore	Cat# AB144P; RRID: AB_262156
Anti-Rat Tbr2	Millipore	Cat# AB2283
Anti-Mouse NeuN	Millipore	Cat# MAB377
Bacterial and Virus Strains		
AAV5-FLEX-TVA-mCherry	UNC Vector Core	N/A
AAV5-FLEX-RG	UNC Vector Core	N/A
RABV-SADΔG-GFP	Salk Institute (GT3)	N/A
AAV5-EF1a-DIO-hChR2(H134R)-EYFP	UNC Vector Core	N/A
AAV5-EF1a-DIO-hChR2(H134R)-mCherry	UNC Vector Core	N/A
AAV5-EF1a-DIO-EYFP	UNC Vector Core	N/A
AAV5-EF1a-DIO-mCherry	UNC Vector Core	N/A
AAV5-EF1a-fDIO-EYFP	UNC Vector Core	N/A
AAV5-hSyn-DIO-hM4Di-mCherry	UNC Vector Core	N/A
AAV5-hSyn-DIO-mCherry	UNC Vector Core	N/A
AAV8-EF1a-fDIO-hM3Dq-mCherry	Stanford University	Dr. Karl Deisseroth
AAV2/9-DIO-GCaMP3	U Pennsylvania	N/A
AAV5-FLEX-taCasp3-TEVp	UNC Vector Core	N/A
Retrovirus-Ubi-GFP-WPRE	Southwestern	Dr. Jenny Hsieh
Chemicals, Peptides, and Recombinant Proteins		
5-Ethynyl-2'-deoxyuridine	Carbosynth	Cat# NE08701
Alexa Fluor 488 Azide	Life Tech	Cat# A10266
Alexa Fluor 594 Azide	Life Tech	Cat# A10270
Clozapine-N-oxide (CNO)	Sigma	Cat# C0832-5MG
Experimental Models: Organisms/Strains		
PV-cre (B6.129P2-Pvalb ^{tm1(cre)Arbr/J})	Jackson laboratory	Stock No: 008069
VGAT-Cre (B6. Slc32a1 ^{tm2(cre)Low/J})	Jackson laboratory	Stock No: 016962
PV-Flp (B6.Cg-Pvalb ^{tm4.1(flpo)Hze/J})	Jackson laboratory	Stock No: 022730
SST-cre (Sst ^{tm2.1(cre)Zjh/J})	Jackson laboratory	Stock No: 013044
Nestin-GFP (B6)	Stony Brook	Dr. Grigori Enikolopov
Lhx6-Cre	Johns Hopkins	Dr. Seth Blackshaw
Software and Algorithms		
ImageJ (Fiji)	http://fiji.sc/	N/A
FV10-ASW 4.2 Viewer	Olympus	N/A

(Continued on next page)

Continued

REAGENT or RESOURCE	SOURCE	IDENTIFIER
GraphPad Prism	GraphPad Software	Prism 7
Huygens Essential	SVI	N/A
NeuroMatic package	N/A	ThinkRandom.com
Igor Pro	Wavemetrics	wavemetrics.com

CONTACT FOR REAGENT AND RESOURCE SHARING

Further information and requests for resources and reagents should be directed to and will be fulfilled by the Lead Contact, Juan Song, Ph.D. (juansong@email.unc.edu).

EXPERIMENTAL MODEL AND SUBJECT DETAILS

Single or double transgenic young adult mice (6–8 weeks, males and females) were used for all the experiments from the following genetically modified mouse lines: PV-cre (B6.129P2-Pvalb^{tm1(cre)Arbr/J}), VGAT-Cre (backcrossed with B6, Slc32a1^{tm2(cre)Lowl/J}), PV-Flp (B6.Cg-Pvalb^{tm4.1(flpo)Hze/J}), and SST-cre (Sst^{tm2.1(cre)Zjh/J}) mice were obtained from the Jackson laboratory; and Nestin-GFP (B6) mice were obtained from Dr. Grigori Enikolopov at Stony Brook University; and Lhx6-Cre (B6) mice were obtained from Dr. Seth Blackshaw at Johns Hopkins University. No immune deficiencies or other health problems were observed in these lines, and all animals were experimentally and drug naive before use. Animals were group housed and bred in a dedicated husbandry facility with 12/12 light-dark cycles with food and water *ad libitum* and under veterinary supervision. Animals subjected to surgical procedures were moved to a satellite housing facility for recovery with the same light-dark cycle. Occasional single-housing was required during cannulation experiments (2–3 weeks). All procedures were conducted in accordance with the NIH Guide for the Care and Use of Laboratory Animals, and with approval of the Institutional Animal Care and Use Committee at the University of North Carolina at Chapel Hill (UNC).

METHOD DETAILS**Stereotaxic surgery**

Young adult mice (6–8 weeks) were anesthetized under 1%–2% isoflurane in oxygen at 0.6–0.8 LPM flow rate. All coordinates were based on values from “The Mouse Brain in Stereotaxic Coordinates” (Second Edition, Paxinos and Franklin, 2001). Virus was injected by microsyringe (Hamilton, 33GA) and microinjection pump (Hamilton), at a rate of 100 nl/min with the following coordinates: MS viral injection (1 μ l): AP +0.75 mm, ML 0.00 mm, DV –3.75 mm; DG viral injection (0.5 μ l): AP –2.0mm, ML \pm 1.5 mm, DV –2.3 mm; Optic fiber (Thorlabs, \varnothing 1.25 mm Multimode LC/PC Ceramic Ferrule, \varnothing 230 μ m Hole Size) and *in vivo* electrodes (Plastics One, two channel-electrodes) were implanted over the DG at AP –2.0 mm, ML \pm 1.5 mm, DV –1.75 mm; guide cannulation (Plastics One, 26GA) were placed at AP –2.0 mm, ML \pm 1.5 mm, DV –1.25 mm (internal cannula, 33GA, DV –1.75 mm). Mice were allowed to recover for 2–3 weeks from the surgery before *in vivo* or *in vitro* experiments. For RV based retrograde tracing mice were injected with 500 nL AAV5-EF1a-FLEX-TVA-mCherry and AAV-CA-FLEX-RG (UNC Vector Core) at a ratio of 1:1 into the right DG. After 3 weeks, same animals had the second injection of 300 nL pseudo-typed RV RABV-SAD Δ G-GFP (Salk Institute Vector Core) using the same coordinates. Then animals were transferred to a quarantined cubicle for special housing and monitoring. 6 days post rabies injection, animals were perfused and brain tissues are collected. For anterograde tracing, mice were injected with 1 μ l AAV5-EF1a-DIO-EYFP (UNC Vector Core) in the MS. and were sacrificed 10–14 days post injection for immunohistochemistry. For *in vivo* optogenetics, mice were injected with AAV5-EF1a-DIO-hChR2 (H134R)-EYFP or AAV5-EF1a-DIO-EYFP (UNC Vector Core) in the MS and implanted with an optical fiber above the DG on the right hemisphere. After 2–3 weeks recovery, free-moving mice were placed in individual 35 \times 45 cm cages. Laser power was adjusted to a final optical fiber output of 10 mW. Unilateral patch cables were connected to rotary commutator (Doric) to avoid twisting. During 8 hours stimulation, animals were provided food on the floor and water bottle on cage wall. The 473 nm blue light paradigm was 5 days of stimulation at 8 Hz for 30 s, with an interval of 5 minutes. Animals were returned to their group-home cages after each stimulation block. On the last day of stimulation, animals were given 4 doses of EdU (40 mg/kg EdU, Carbosyht) at 2 hour intervals by intraperitoneal injections, and perfused 2 hours after the last injection of EdU. For *in vivo* chemogenetics, mice were injected with AAV5-hSyn-DIO-hM4Di-mCherry or AAV5-hSyn-DIO-mCherry (UNC Vector Core) in MS and implanted with a guide cannula (Plastics One, 26GA) above the DG. Animals were allowed to recover under single-housing conditions to prevent damage to the guide cannula for 2–3 weeks. Mice were slightly anesthetized with isoflurane on the stereotaxic apparatus and connected to the cannula infusion system, including internal cannula (Plastics One, 33GA), tubing, microsyringe (Hamilton, 26GA) and microinjection pump. Water-soluble CNO (Sigma) was infused through cannula to the DG (300 nl, 1 mM) at a rate of 50 nl/min. Internal cannula remained positioned in the brain for 5 minutes after the infusion before removal. Only one CNO infusion was given to each animal. The first 40 mg/kg EdU (Carbosyht) intraperitoneal injection was given immediately following the

infusion, and then again every 2 hours. Animals were sacrificed and perfused for tissue processing (described below) 8 hours after the CNO delivery. Similar procedures were applied for VGAT-Cre::PV-Flp *in vivo* experiment. AAV5-hSyn-DIO-hM4Di-mCherry was injected to MS, and AAV8-EF1a-fDIO-hM3Dq-mCherry (Stanford) or AAV5-EF1a-fDIO-YFP was injected to DG along with the cannulation above DG. For Caspase3-mediated ablation, mice were injected with AAV5-FLEX-taCasp3-TEVp or AAV5-EF1a-DIO-YFP (UNC Vector Core) into the MS, and mice were sacrificed at 1, 2, or 6 weeks after viral injection for immunohistochemistry, quantification. For retroviral birth dating, mice were injected with AAV5-FLEX-taCasp3-TEVp or AAV5-EF1a-DIO-YFP (UNC Vector Core) into the MS and followed with a second retrovirus injection at 4 wpi. Mice were sacrificed 2 weeks after retrovirus injection. For slice recording, viral infections were conducted in similar ways. Additional AAVs including AAV5-EF1a-DIO-hChR2 (H134R)-mCherry, AAV5-EF1a-DIO-mCherry, AAV5-EF1a-fDIO-EYFP (UNC Vector Core) were injected into the MS or DG of the adult mice for different experiments.

Immunohistochemistry

Mice were anesthetized with ketamine, and perfused with ice-cold 4% paraformaldehyde (PFA) in PBS. Brains were collected and placed in 4% PFA overnight, and switched to 30% sucrose for 2-3 days until they were fully submerged. Brains were sectioned on a microtome at the thickness of 40 μm , and stored in the anti-freeze solution at -20°C for further usage.

For staining of floating sections, brain sections were washed twice with TBS, followed by permeabilization with 0.5% Triton-100 TBS for 20 minutes. After washed with TBS+ (TBS with 0.05% Triton-100) for 5 minutes and blocked with 3.5% donkey serum in TBS+ for 30 minutes. Sections were incubated in the primary antibody overnight at 4°C on the shaker. On the second day, brain sections were washed with TBS+, and then incubated with secondary antibody at room temperature for 2 hours.

For quantifications of NSCs, coronal brain sections (40 μm) through the entire DG were collected in serial order. Immunostaining was performed on every 6th section encompassing the anterior to posterior end of the DG as previously described (Kim et al., 2009; Song et al., 2012b). For the combination of nestin and EdU staining, antigen retrieval was required. Tissues were first mounted on charged slides and air-dried for 5-10 minutes. Then slides were placed into a 1 mL tip box filled with preheated citrate buffer. The tip box was boiled in the microwave for 7 minutes with brief pauses to avoid massive bubbling. After the heat retrieval, the tip box was removed from microwave to ice to cool down to the room temperature. Slides were then removed and air-dried for 5 minutes. Hydrophobic PAP pens were used to define a staining border around the sections. For EdU labeling, slides were incubated in the EdU click reaction buffer (0.1 M Tris, 0.5–1 mM CuSO₄, 30 μM 488 Alexa azide fluorescent-azide, and 50–100 mM ascorbic acid) for one hour. After washing, the antibody staining steps were similar to the ones described for floating sections.

Imaging

Confocal images were acquired by Olympus FLUOVIEW1000 confocal microscopy, under 40x Oil (NA1.30), XY-resolution 0.4975 $\mu\text{m}/\text{pixel}$, Z-resolution 1.0 or 1.5 $\mu\text{m}/\text{slice}$. Tiled images were acquired based on locations of the fluorescent signals, and images were stitched after acquisition using the Olympus FluoView imaging software. Brightness and contrast were adjusted with ImageJ. Whole-brain input screening images were acquired and stitched by UNC Translational Pathology Laboratory.

Slice Electrophysiology

Adult mice housed under standard conditions were used at 2-4 weeks post AAV injection for slice preparation. Animals were anesthetized under isoflurane and briefly perfused intra-cardially with 10 mL of ice-cold NMDG solution (Ting et al., 2014) containing (in mM): 92 NMDG, 30 NaHCO₃, 25 glucose, 20 HEPES, 10 MgSO₄, 5 sodium ascorbate, 3 sodium pyruvate, 2.5 KCl, 2 thiourea, 1.25 NaH₂PO₄, 0.5 CaCl₂ (pH 7.3, 300 mOsm, bubbled with 95% O₂ and 5% CO₂). The brains were then quickly removed into additional ice-cold NMDG solution for slicing. Transverse slices (Otmakhov et al., 2004) were cut using a Leica VT1200S vibratome at 280 μm thickness, and warmed to 36.5°C for 10 minutes. Slices were transferred to room temperature ($22-24^{\circ}\text{C}$) HEPES holding solution (Ting et al., 2014) containing (in mM): 92 NaCl, 30 NaHCO₃, 25 glucose, 20 HEPES, 5 sodium ascorbate, 3 sodium pyruvate, 2.5 KCl, 2 thiourea, 2 MgSO₄, 2 CaCl₂, 1.25 NaH₂PO₄, (pH 7.3, 300 mOsm, bubbled with 95% O₂ and 5% CO₂) for 1 - 2 hours.

Electrophysiological recordings were obtained at $22-24^{\circ}\text{C}$ in artificial CSF containing (in mM): 125 NaCl, 26 NaHCO₃, 20 glucose, 2.5 KCl, 2 CaCl₂, 1.3 MgCl, 1.25 NaH₂PO₄, (pH 7.3, 300 mOsm, bubbled with 95% O₂ and 5% CO₂) on a Scientifica SliceScope. GFP⁺ NSCs or YFP⁺ PV interneurons within the sub-granule zone were visualized by DIC and fluorescence microscopy. Mature granule cells in the mid-to-outer granule cell layer were identified by DIC microscopy. Microelectrodes (3–6 M Ω) were pulled from borosilicate glass capillaries (WPI) and filled with high chloride internal solution containing (in mM): 140 KCl, 10 EGTA, 8 HEPES, 2 Mg₂-ATP (pH 7.3, 310 mOsm) (Overstreet and Westbrook, 2001). Additional chemicals were used at the following final concentrations in the bath as indicated: bicuculline (50 μM), CNQX (10 μM) and AP5 (100 μM). All chemicals were purchased from Sigma except bicuculline, CNQX, AP5 (Tocris) and ω -agotoxin TK (Alomone Labs). Experiments using ω -agotoxin TK were pre-incubated in the antagonist for 1 hour before recording.

Data were collected using a Multiclamp 700B amplifier and digitized with a DigiData 1440A (Axon Instruments) at 10 kHz using pClamp10 software. The whole-cell patch-clamp configuration was employed in voltage-clamp mode ($V_m = -65$ to -80 mV depending on the resting membrane potential of the cell type). To stimulate ChR2 in VGAT⁺ terminals, light pulses

(1 ms to 15 s) were generated by a pE-100 (CoolLED) 470 nm LED and triggered via TTL control through the acquisition software, illuminated through a 40X objective.

Ca²⁺ imaging

GCaMP3 (Tian et al., 2009) was selectively expressed in adult dentate PV or SST neurons through AAV-mediated, Cre-dependent expression (AAV2/9-EF1a-FLEX-GCaMP3 (U Penn Vector Core)) in adult PV-Cre or SST-Cre mice (Atasoy et al., 2008; Cardin et al., 2009; Sohal et al., 2009). Acute brain slices (275 μ m) were prepared as for electrophysiology. Calcium imaging was performed on a Zeiss (Germany) LSM 510 confocal imaging system with a 40X water immersion objective (Achromplan, 0.8 numerical aperture; Zeiss). Different groups of cells were treated with muscimol (10 μ M) and then ionomycin (10 μ M) without or with pretreatment of La³⁺ (50 μ M), ω -Agatoxin TK (100 nM) or bumetanide (20 μ M). Cells were excited at 488 nm, and Fluo-4 signal was collected at 505–550 nm. Images were acquired every 5 s and analyzed using NIH ImageJ software.

Time-locked video-EEG recording

6–8 weeks after Cas3/YFP virus injection, mice were connected to a tethered video-EEG recording system (Cambridge Electronic Design Limited, UK). A commutator (PlasticsOne, Roanoke, VA) allowed mice to move freely during recording. Time-locked video EEG was recorded for 48hr continuously under a 12 hour light/dark cycle with food and water provided *ad libitum*. Discrete spontaneous seizures and epileptiform activity were inspected by an investigator who is blinded to genotype by reviewing the video-EEG using Spike2 software.

Flurothyl-induced seizure

Mice were tested individually within an air-tight glass chamber (2 L) in a ventilated chemical hood. Mice were allowed to habituate to the chamber for 1 minute prior to the administration of 10% flurothyl (bis(2,2,2-trifluoroethyl) ether) in 95% ethanol, which was infused through a 5 mL syringe onto a filter paper suspended at the top of the chamber at a rate of 200 μ l/min. Resultant seizure behaviors were recorded using a video camera and the following events were scored blind to genotype: 1) latency to the first myoclonic jerk (i.e., brief, but severe, contractions of the neck and body musculature occurring while the mouse maintains postural control); 2) latency to the first generalized seizure (i.e., convulsions resulting in a loss of postural control). Upon observation of generalized seizure, the lid of the chamber was immediately opened, exposing the mouse to fresh air, thereby facilitating cessation of the seizure.

QUANTIFICATION AND STATISTICAL ANALYSIS

General

Mice from both sexes were used for all experiments, as our previous studies have established that sex difference did not appear to contribute to observed statistical variation (Song et al., 2012b, 2013). At least two replications were used for each experimental paradigm and combined for analysis. Surgical strategies were carefully designed to combine different groups of mice in the same cage. Mouse identity and experimental manipulation was coded to allow for blind imaging and analysis of the immunohistochemical quantifications. Sample sizes were based on previous publications with extra samples to account for potential excluded data. Mice with off-target viral injections or expression outside the area of interest were excluded from analysis after post hoc examination of fluorescence expression. Statistical analysis was performed with two-tailed unpaired Student's t test or Kolmogorov-Smirnov test to determine the statistical significance. Datasets were confirmed to be normally distributed by the Shapiro-Wilks test and quantile-quantile (q-q) plot in SAS software. Sample size was represented by 'n' and reported in figure legends. 'n.s' indicates no significant difference ($p > 0.05$). Values represent mean \pm SEM. All data were analyzed in GraphPad Prism7.

Cell quantification

Slide identities were blinded with tape after immunostaining to avoid bias during imaging and quantification. For nestin and EdU quantification, whole tiling DG images were acquired, and quantified manually through z stacks. MS cell quantifications were done manually by single plane or z stack counting. For DCX quantification, DCX measurements were processed by Huygens Essential software (Scientific Volume Imaging SVI). Confocal z stacks were imported to Huygens, and analyzed by the 'Object Analyzer' plugin. ROIs were defined along the bottom 1/3 of the granule cell layer manually based on each individual DG tiling image, to cover all DCX⁺ cells. The thresholding values were as follows: Threshold 20%, Seed 10%, and Garbage volume 200. The threshold settings were constant through all the images. The data were represented in voxel volume for all the 3D-pipes measured in the ROIs, and were normalized with the DG volume (calculated in ImageJ). For retrovirus analysis, dendrites were analyzed using the plugin "Simple Neurite Tracer" in ImageJ (Schindelin et al., 2012; Winkle et al., 2016). Sholl analysis was performed by counting the number of crossings by dendrites of concentric circles originating at the soma with increasing radii of 10 μ m in ImageJ (Winkle et al., 2016).

Slice Electrophysiology

Electrophysiology traces were analyzed using a combination of the NeuroMatic package (by Jason Rothman, ThinkRandom.com) and custom built analysis routines, written for Igor Pro (Wavemetrics). Electrophysiology statistics were confirmed normal and random by Igor Pro Stats package before running Student's t test or Kolmogorov Smirnov test (in Igor Pro).

Ca²⁺ imaging

The change in Ca²⁺ signal was determined by $\Delta F/F$ ($\Delta F/F = [(F_1 - B_1) - (F_0 - B_0)] / (F_0 - B_0)$), which was normalized to the mean fluorescence intensity measured at the baseline condition (set as 0%) and after the ionomycin treatment (set as 100%).

DATA AND SOFTWARE AVAILABILITY

ImageJ is an open source software for image analysis. Some scripts used in Igor Pro for electrophysiology analysis were custom made for particular analysis routines. All others are commercial software. See the Key Resources Table for details.